AN ABSTRACT OF THE THESIS OF

Spencer H. Harper for the degree of Master of Science in Civil Engineering presented on August 31, 2020.

Title: Data Assimilation using Synthetic-Aperture Radar Imagery for Bathymetry Inversion at the Mouth of the Columbia River.

Abstract approved: ____

H. Tuba Özkan-Haller

Synthetic-aperture radar (SAR) imagery can provide wavenumber and frequency data to generate bathymetry estimates for locations where limited access or extreme ocean conditions can make standard bathymetry survey techniques difficult or impossible. The availability of SAR data could allow for regular bathymetry estimates of navigational channels providing insight into dredging intervals and efficiency. Estimates would also be of value in military applications to gather information about denied areas. Strong currents, extreme ocean conditions, and significant discharge from the river make the Mouth of the Columbia River (MCR) on the US West Coast a challenging location for bathymetry estimation. Successful bathymetry estimations at the Mouth of the Columbia River could provide opportunities to apply this method to other, less challenging locations.

This study assimilates SAR wave number observations with hydrodynamics characteristics generated from numerical models. A Regional Ocean Modeling System (ROMS) one-way coupled to a Simulated Waves Nearshore model (SWAN) is used to model the wave-current dynamics and provide wave characteristics and current velocities for an estimated bathymetry. Solving the dispersion relationship for the change in wavenumber with respect to water depth allows us to implement weighted least squares method with a Bayesian estimation to minimize the error between the model predicted and observed wavenumbers using covariance matrices.

This framework allows for a best guess bathymetry of the Mouth of the Columbia River to be updated by assimilating solely SAR wavenumber observations.

Our goals are to determine if SAR observations from four individual images can be assimilated to estimate a bathymetry that qualitatively reproduces the location and depths of the bathymetric features in the actual bathymetry, explore sensitivity of variations in assimilated frequency, and to establish limitations of this method and SAR observations used for bathymetry inversion. The framework was tested using model-derived observations that mimicked those collected via SAR. The assimilation using the model derived observations illustrated that high quality observations, a highly-skilled model, and ample spatial coverage can result in estimates of the pronounced features of the MCR bathymetry. To utilize the SAR observations for assimilation, it was necessary to assign a frequency to the observed wavenumbers. Assigned frequencies were determined by comparing wave directions between the observations and an offshore buoy. Under certain conditions the framework provided improvements to the initial bathymetry when assimilating the SAR observed wavenumbers and their assigned frequencies. The method could occasionally predict the location and extent of features including the MCR navigational channel, Peacock Spit, Clatsop Spit, and a dredge disposal site. Sensitivity to assigned frequencies in the assimilation results was explored and it was determined that the frequencies observed by the buoy (or very similar to those) provided the best bathymetric results. The results of this method were limited by the presence of breaking waves in the SAR images and spatial coverage of observations.

Data Assimilation using Synthetic-Aperture Radar Imagery for Bathymetry Inversion at the Mouth of the Columbia River

by

Spencer H. Harper

A THESIS

submitted to

Oregon State University

in partial fulfillment of
the requirements for the
degree of

Master of Science

Presented August 31, 2020
Commencement June 2021

Master of Science thesis of Spencer H. Harper presented on August 31, 2020

APPROVED:

Major Professor, representing Civil Engineering

Head of the School of Civil and Construction Engineering

Dean of the Graduate School

I understand that my thesis will become part of the permanent collection of Oregon State University libraries. My signature below authorizes release of my thesis to any reader upon request.

Spencer H. Harper, Author

ACKNOWLEDGEMENTS

I have been very lucky to have the opportunity to work with some incredibly talented and intelligent individuals as a part of this project. I would like to express my sincerest gratitude and appreciation to my advisor Tuba Özkan-Haller for her time, patience, ideas, and guidance in preparation of this thesis. I would also like to thank Greg Wilson and Chris Wackerman; each of them was immensely helpful in my quest to understand both the SAR imagery and the inversion method. My sincere appreciation goes to Chuan Li who helped me through all parts (research, thesis, homework, etc.) of my graduate school career; it would have been a lot more painful without you. Thank you to David Honegger and Jeff Wood for providing background information and aerial imagery for the figures used in this thesis. I would like to thank my committee members Mick Haller, Peter Ruggiero, and Emily Shroyer for their time and contributions to this thesis.

I have enjoyed my time here in Corvallis more than I thought I ever would have; I am grateful to all those in the Coastal engineering program who made my time here memorable. I would like to thank my family and for their support. Finally I would like to express my appreciation to Adriana for all she has done to support me especially during our time here in Corvallis.

This research was funded by the Office of Naval Research.

TABLE OF CONTENTS

Page

TABLE OF CONTENTS (Continued)

Page

LIST OF FIGURES

LIST OF FIGURES (Continued)

LIST OF FIGURES (Continued)

Figure Page

LIST OF FIGURES (Continued)

LIST OF FIGURES (Continued)

LIST OF TABLES

<u>Table</u> <u>Page</u>

Chapter 1: Introduction

The Mouth of the Columbia River (MCR) is a critically important coastal inlet located in the Pacific Northwest of the United States. The MCR provides passage for $20 billon of trade as well as supports the local economy in Astoria, OR, and the numerous ports located along the Columbia River in both Oregon and Washington. It is important that the navigational channel is maintained to allow the 42 million tons of annual cargo to pass through the inlet and support more than 40,000 trade-dependent jobs (USACE, 2012). This necessity has required the MCR to be a heavily engineered inlet with a convergent jetty system and the need to dredge three to five million cubic meters of sediment annually (J. Gailani et al., 2019). The navigational channel is over-dredged each year by 1.5 m to account for the inability to dredge in the winter due to the energetic conditions (Moritz et al., 2007).

Tidal inlets, in general, are a challenging setting to make observations due to high flowrates, sediment transport, and morphological change (Elias et al., 2012). The MCR is subject to large waves, strong currents, and variable bathymetry or depth; these characteristics make it a challenging environment to predict and maintain. Bathymetry estimation at tidal inlets is a topic of interest for coastal scientists and engineers as tidal inlets are subject to a large amount of morphodynamic change (Barnard et al., 2012). Having a method to provide reliable bathymetric estimates using remote sensing technology could provide valuable information that would show almost real-time bathymetric change after the annual dredging is complete and provide insight into how the channel changes throughout the year. The value of bathymetry estimation using remote sensing has been acknowledged by the military, as well, as surveys of navigational inlets in restricted areas are often impossible to achieve (Moghimi et al., 2016).

Assimilating information about waves or currents, or both, for bathymetric estimation has shown promising results in riverine, nearshore, and tidal inlet applications. Bathymetry estimation is possible by assimilating both surface currents and wave characteristics that are observed via in situ measurements or remote sensing techniques. For example, Landon et al. (2014) developed bathymetry estimates by assimilating velocity observations collected from surface drifters in the Kootenai River. Wilson et al. (2014) showed the ability to improve nearshore bathymetry estimates by assimilating in situ and remote sensing observations of frequency-wavenumber pairs and alongshore currents. Moghimi et al. (2016) assimilated both wave and surface current information to improve bathymetry estimates at tidal inlets. These aforementioned studies are based on an ensemble-based data assimilation framework presented by Wilson et al. (2010), and use a combination of in situ and remote sensing data. It is our intention to determine if assimilating solely remote sensing observations (from Synthetic-aperture radar [SAR imagery]) of wave kinematics can improve bathymetric estimates using a hybrid assimilation method similar to Wilson et al. (2010) and Wilson & Özkan-Haller (2012). The method presented here will not rely on an ensemble-based framework and will therefore, allow for computationally efficient and quick production of bathymetric estimations.

Prior attempts have been made using remote sensing data; both SAR (Yu et al., 2016) and marine X-band radar (Honegger et al., 2020; Zuckerman & Anderson, 2018) to obtain estimates of bathymetry at tidal inlets. Direct inversion of the dispersion relationship using X-band radar and the cBathy algorithm (Holman et al., 2013; Plant et al., 2008) was completed by Honegger et al (2019, 2020) at the MCR and New River Inlet, NC. Bathymetry estimates at the MCR generated a root-mean-squared-error (RMSE) of 4.20 m in the river mouth when compared to the same true bathymetry (Akan et al., 2018) used in this study. Herein we will be using solely satellite based remote sensing data and inverting the dispersion relationship to generate our bathymetric estimates at the MCR.

In linear wave theory, the dispersion relation dictates how the frequency and wavenumber of a wave component are related to the bathymetry and currents at a particular location. This relationship can be inverted using data assimilation methodologies to estimate a depth using estimated or observed values of angular frequency, wavenumber, wave direction, and currents. We will show how we have assimilated observations derived from SAR imagery to estimate bathymetry using weighted least squares with a Bayesian estimation to minimize the error between observed wavenumbers and those predicted by a numerical model. Our goals are to determine if SAR observations can be assimilated to estimate a bathymetry that qualitatively reproduces the location and depths of the bathymetric features in the actual bathymetry, explore sensitivity of variations in assimilated frequency, and to establish limitations of this method and SAR observations used for bathymetry inversion.

Chapter 2: Methods

2.1. Study Location

The Mouth of the Columbia River is located in the Pacific Northwest of the United States, where the Columbia River outlets to the Pacific Ocean. The Columbia River serves as the border between Washington state and Oregon. The inlet is stabilized by three rubble-mound jetties; north jetty, south jetty, and jetty A which all extend from tidal shoals on either side of the inlet. The Columbia River jetties were constructed between 1885 and 1917, with the south jetty constructed between 1885 and 1895 and the north jetty constructed between 1913 and 1917. The south jetty extends across Clatsop Spit towards the inlet; the jetty was originally constructed with a length of 6.8 km but was extended by an additional 4 km between 1903 and 1913. North jetty traverses Peacock Spit on the Washington side and has a total length of 3.8 km. The construction of the Columbia River jetties reduced the inlet size from 9.6 km to 3.2 km which in turn increased the velocity of the tidal currents in the inlet and deepened the channel (Kaminsky et al., 2010).

An 8-km long 905-m wide and 17-m deep navigational channel located between the jetties is maintained via dredging by the US Army Corp of Engineers (USACE). Dredge material is disposed of at one of three beneficial use sites (Shallow Water Site, SWS; North Jetty Site, NJS; and South Jetty Site, SJS) and one Ocean Dredged Material Disposal Site (ODMDS), identified as ODMDS F. Several historical ODMDSs (A, B, and E) exist and can be seen in Figure 1 along with the current deep water disposal site ODMDS (Site F). Sites A and B are of importance for this study as they are existing bathymetry features that can be used to assess the performance of the inversion method. ODMDS (Site A) is located to the southwest of the tip of the South Jetty; disposal at site A has not taken place since 1994 due to reports that the mound was causing waves to steepen, amplify and break in the vicinity of the channel (J. Z. Gailani et al., 2003). It was estimated in 1995 that the disposal mound at site A will be dispersed outside of the area boundaries in approximately 20-40 years' time. In contrast, ODMDS B (site B) is located almost directly west of the inlet and is not considered to be a dispersive site (J. Z. Gailani et al., 2003); it can clearly be seen in the bathymetry used for this study.

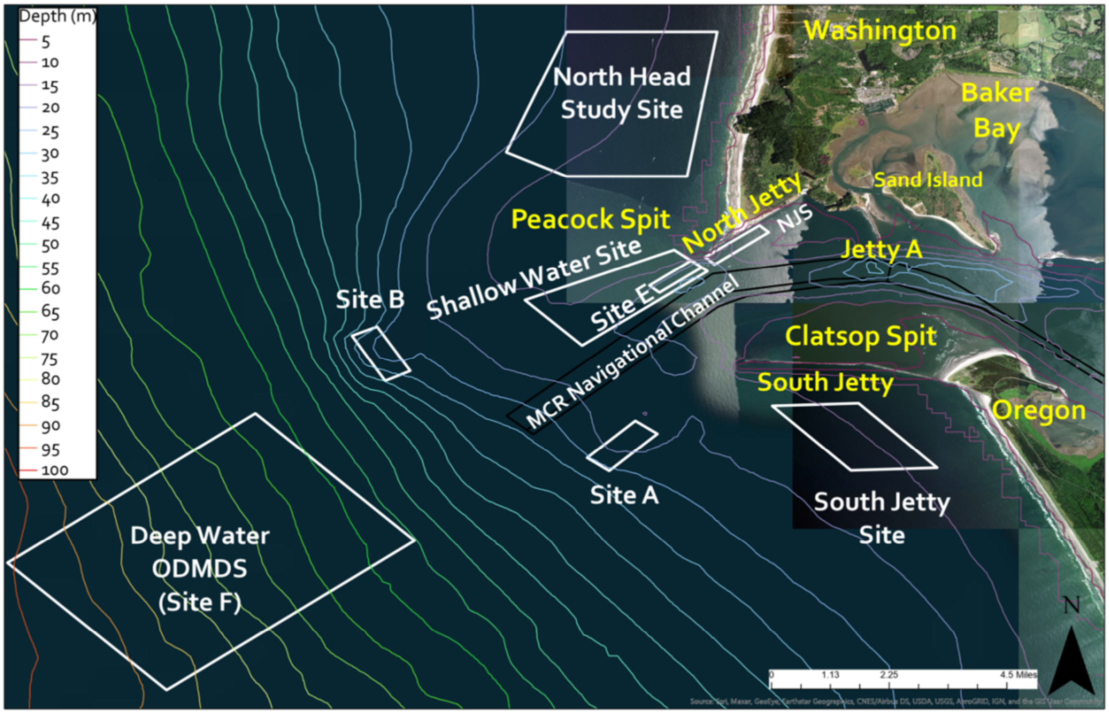

Figure 1: The Mouth of the Columbia River outlets to the Pacific Ocean between two rubble-mound jetties, the study area features multiple shoals, spits, and dredge material disposal sites

The bathymetry at the Mouth of the Columbia River is characterized by a few key features that can be seen in Figure 1; the navigational channel, Peacock Spit, Clatsop spit, and ODMDS Site A and B. The navigational channel begins with a northwestern trajectory as it traverses the Lower Columbia River Estuary. The channel then widens and transitions to the MCR navigational channel when it reaches Sand Island. The channel points west from Jetty A before taking on a southwestern direction and exiting the inlet between the north and south jetties. Peacock Spit is located on the Washington side of the inlet and abuts the north jetty and extends from Benson beach in the offshore direction. Clatsop Spit is located on the Oregon side of the inlet and follows along the south jetty while extending into the southern portion of the channel. ODMDS A and B are historical disposal sites located southwest of the tip of the south jetty and due west of the inlet mouth respectively; the disposal sites are distinct features that diverge from the surrounding bathymetry. We will qualitatively evaluate the depth and extent of these features within the bathymetry estimates, and we will use these key features to gauge the performance of the estimate.

The wave climate of the Pacific Northwest is severe and associated with large wave heights and long period swells generated by large fetch areas in the North Pacific (Tillotson & Komar, 1997). The wave climate at the Columbia River inlet varies with season, typically in the winter time the inlet experiences waves with an average height of 3 meters, 12 to 13 second periods, and a wave approach direction of west-southwest. In the summer the average wave height is closer to 1.2 meters, with an average period of 8 seconds, and an approach direction from the west-northwest (Ruggiero et al., 2005).

The Columbia River watershed includes parts of British Columbia, Alberta, Washington, Oregon, Montana, Idaho, Wyoming, Nevada, and Utah for a total drainage area of approximately 668,000 km^2. Mean monthly river discharge varies from 3,500 to 9,600 m^3/s throughout the year, and tidal velocities range from 1 m/s during flood to 2 m/s during ebb conditions (Akan et al., 2017). A plume generated by the river outflow extends to the continental shelf and is responsible for impacts to the local salinity, temperature distribution, and algae blooms (Akan et al., 2017). It has been shown that the tidal currents at the MCR impact the waves (Gonzalez et al., 1985) and during ebb tides can increase the wave height by a factor of two (Elias et al., 2012). These strong wave-current interactions provide challenging conditions for observations and can often force wave breaking to happen at the mouth of the inlet.

2.2. Model Description

The coupled ocean-atmosphere-wave-sediment transport (COAWST) modeling system (Warner et al., 2010) applied by Akan et al. (2017) was used to generate the hydrodynamic characteristics necessary to complete the bathymetric inversion. The COAWST model includes a Regional Ocean Modeling System (ROMS) (Shchepetkin & McWilliams, 2003, 2005) one-way coupled to a Simulated Waves Nearshore model (SWAN) (Booij et al., 1999). Only the wave and current components of COAWST model were used. The work herein is primarily based on the validated simulations of Akan et al. (2017). The model run duration was updated to encompass the period of time during which SAR observations took place. Model runs were completed for two bathymetric configurations; an actual observed (true) bathymetry, and a simplistic first guess (prior) bathymetry. The true bathymetry is described in Akan el al., (2018), and prior bathymetry was generated by spatially smoothing the true bathymetry. A smoothing length scale was applied to a rectangular area that covered the inlet and the surrounding area offshore of the inlet. The horizontal smoothing length scale ranged from 500 to 6,000 m and increased away from the rectangular boundary (D. Honegger, College of Engineering, Oregon State University, 2020, personal communication). The resulting prior bathymetry includes a relatively flat region with no channel present in the area between the north and south jetties. ODMDS A and B are no longer present in the prior bathymetry, the westerly extend of Clatsop Spit has been reduced and there is no sign of Peacock Spit (see Figure 2).

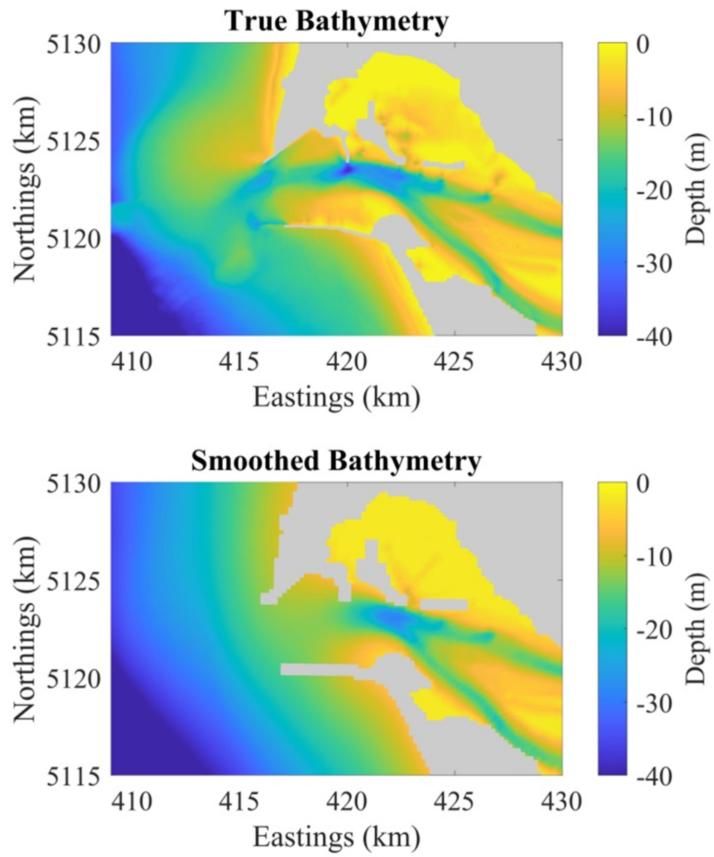

Figure 2: True Model Bathymetry as described in (Akan et al., 2018) and the smoothed "prior" model bathymetry created by applying smoothing length scales to a rectangular area near the MCR to remove key bathymetric features

2.3. Data Observations

36 Synthetic Aperture Radar Images of the MCR were collected by the COSMO-SkyMed and TerraSAR- X and satellites between May 21, 2013 and June 14, 2013. The images were collected as part of a larger field experiment conducted at the Mouth of the Columbia River (Gelfenbaum et al., 2013). These images were post-processed by Dr. Christopher Wackerman at the Naval Research Laboratory to generate wave characteristics. The SAR images selected for analysis and assimilation were collected on: May 21, 2013 13:47:33 UTC, May 29, 2013 02:26:20 UTC, May 30, 2013 02:26:20 UTC, and June 08, 2013 02:14:14 UTC. The images were selected because they had good clarity and showed a strong wave signature. Each SAR image captures an area of approximately 2 square kilometers and provides a total of approximately

800 observation points per image. The SAR image captures surface waves and the wavelengths of these waves can be estimated by directly measuring the distance between wave peaks using a Fourier transform method. A SAR image has an associated dwell time, which is the period of time it takes for the SAR to capture the image as it travels past the target image location. Hence, it is possible to estimate the rate at which the waves are traveling and therefore their period. The dwell time for an observation point is often only 1-2 second and this is a significantly shorter time period when compared to the average period of waves at the MCR of 8 -14 seconds. Therefore, the estimated frequency can have a large amount of error associated with it due to the SAR only observing the wave traveling over a relatively short distance during the image capture.

Wavenumber observations are generated by moving a small sample window across the image and completing a two-dimensional Fast Fourier Transform (FFT) to locate the spectral energy peaks. This process was completed by Dr. Christopher Wackerman, and the data was provided for assimilation. For further information regarding SAR observations of ocean waves it is recommend that the reader reviews Lyzenga (1988). Generating wave characteristics from SAR images is limited if the Fourier transform window does not encompass any wave modulations, breaking waves are present, or if image noise is present. The peak spectral signal to noise ratio (SNR) was used as a metric to determine the quality of wavenumber observations by the SAR. Along with the wavenumber-frequency pairs, the following additional data was included with the observational data set; spectral energy, SNR, latitude, and longitude. For each FFT window a spatial spectrum is generated by averaging the intensity of each FFT. Using these spatial spectra an overall spectral peak value can be identified for the entire image. To define a local peak a scale factor is used; the scale factor is a cut-off value established as ninety percent of the overall maximum spectral peak value. At each observation point the scale factor allowed for the wavenumber-frequency pair that was associated with the largest spectral value to be selected for assimilation. This approach resulted in a single wavenumber-frequency pair at each spatial data point for a majority of the time. In the event that more than one pair was associated with a point, the pair with the largest SNR was selected for assimilation. The SAR observations generate wavenumber component (k_x and k_y) values, and these values are defined with the following orientation in the SAR image. k_x is positive to the right and k_y is positive when pointed towards the bottom of the image. The SAR sensor has a look direction that is reported relative to degrees from true North.

The SAR-observed wave frequency has a significant amount of associated noise and it was determined that the observed frequency would not be suitable for use in the assimilation (C. Wackerman, Naval Research Laboratory, 2019, personal communication). This was confirmed in trial assimilations where the SAR observed wavenumber-frequency pairs were used and an inverted bathymetry was produced that was unrealistic and showed little similarity to the true bathymetry. To successfully invert the bathymetry by assimilating the SAR wavenumber observations, it will be necessary to estimate the correct wave frequency for each observation.

2.4. Environmental Conditions

It is important to understand the environmental conditions at the Mouth of Columbia River during each image collection as these provide background information about the conditions that are impacting the wave kinematics and will impact the assimilation results. Environmental conditions are observed by a buoy located 20 nautical miles offshore of the MCR, the buoy is operated by the National Oceanic and Atmospheric Administrations (NOAA) National Data Buoy Center (NDBC). NOAA buoy 46029 is located in 134 meters of water depth and records detailed wave and atmospheric conditions including but not limited to; wave height, wave direction, wave period, wind speed, wind direction, and atmospheric pressure. The buoy also produces spectral wave data that will be used in the wave direction filtering process discussed later on. An estimation of surface currents and water levels during each SAR image collection can be obtained using the ROMS component of the COAWST model. The ROMS model results are preferable to the observations of the NOAA tide gauge located in Astoria, OR because the tide gauge is approximately 8 km upriver from the MCR and therefore allows for a tidal lag to be present. Using the observations from the offshore buoy and the ROMS-predicted currents and water levels, we can obtain an overall idea of the environmental conditions that were present during the SAR image capture.

2.4.1. May 21, 2013 13:47:33 UTC

The May 21, 2013 13:47:33 UTC image was collected during the beginning of the flood tide. Mild currents were present between the north and south jetties with a maximum velocity of around 1 m/s. The energy spectrum from the buoy shows a bimodal spectrum at both the 13:00 UTC and 14:00 UTC measurements. The spectral peaks between the two measurements fluctuate between 0.0625 Hz and 0.1 Hz. Wind speeds are steadily increasing during the time of the SAR observation. The SAR image clearly shows two crossing wave trains and no discernable current front.

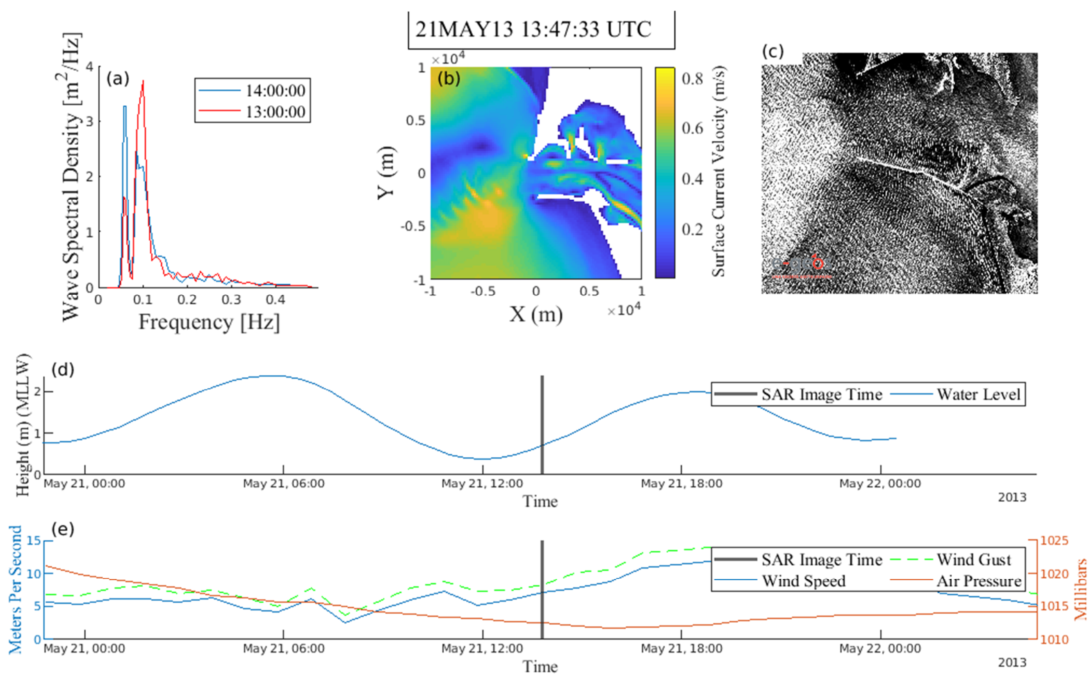

Figure 3: Environmental Conditions for 21 MAY 2013 13:47:33 UTC SAR image including (a) NOAA buoy 46029 energy spectrum (b) ROMS generated surface currents (c) SAR image (d) ROMS generated water level for MCR (e) Wind speed and Air Pressure from NOAA buoy 46029

2.4.2. May 29, 2013 02:26:20 UTC

The May 29, 2013 02:26:20 UTC image was collected during an ebb tide. Strong currents are present during the image capture with a majority of area between the jetties experiencing velocities of at least 1m/s. The energy spectrum shows a predominant peak associated with a frequency of 0.12 Hz and a smaller peak with a frequency of 0.08 Hz. Wind speeds are between 7-9 m/s, and the air pressure is falling during the time of the observation.

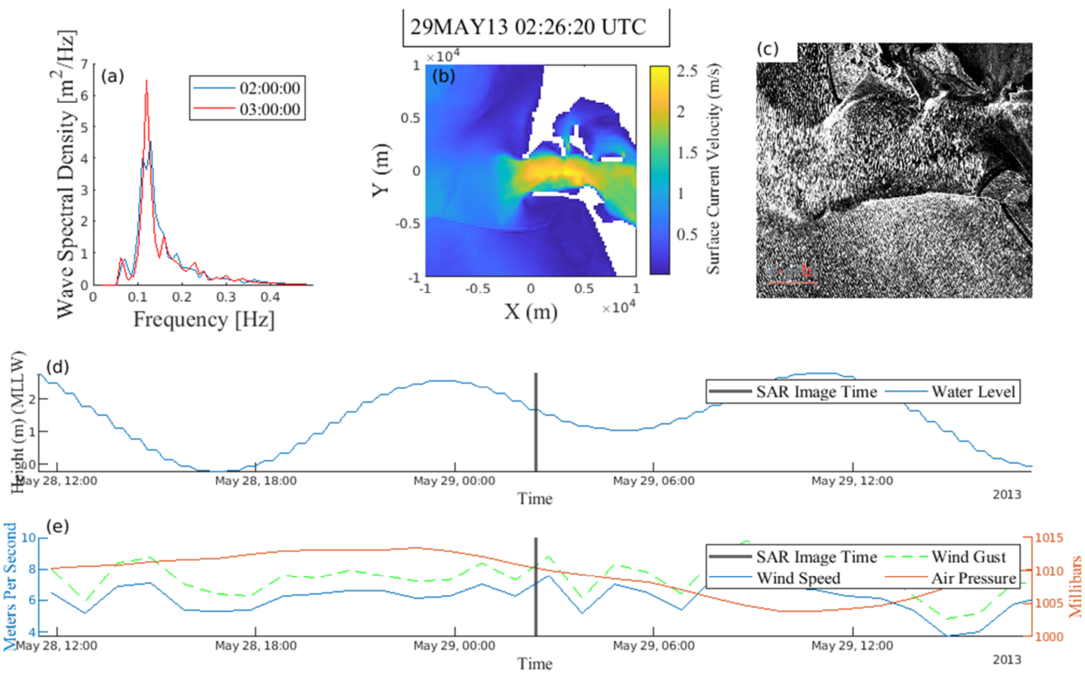

Figure 4: Environmental Conditions for 29 MAY 2013 02:26:30 UTC SAR image including (a) NOAA buoy 46029 energy spectrum (b) ROMS generated surface currents (c) SAR image (d) ROMS generated water level for MCR (e) Wind speed and Air Pressure from NOAA buoy 46029

2.4.3. May 30, 2013 02:20:17 UTC

The May 30, 2013 02:26:20 UTC image was collected during the beginning of an ebb tide. Weak currents are predicted with a velocity range between the jetties of 0-0.5 m/s. The offshore energy spectrum shows a broad spectral peak with a frequency of 0.12 Hz, and a smaller peak around 0.08 Hz. Air pressure is steadily increasing, and wind speeds are falling during the SAR image capture time.

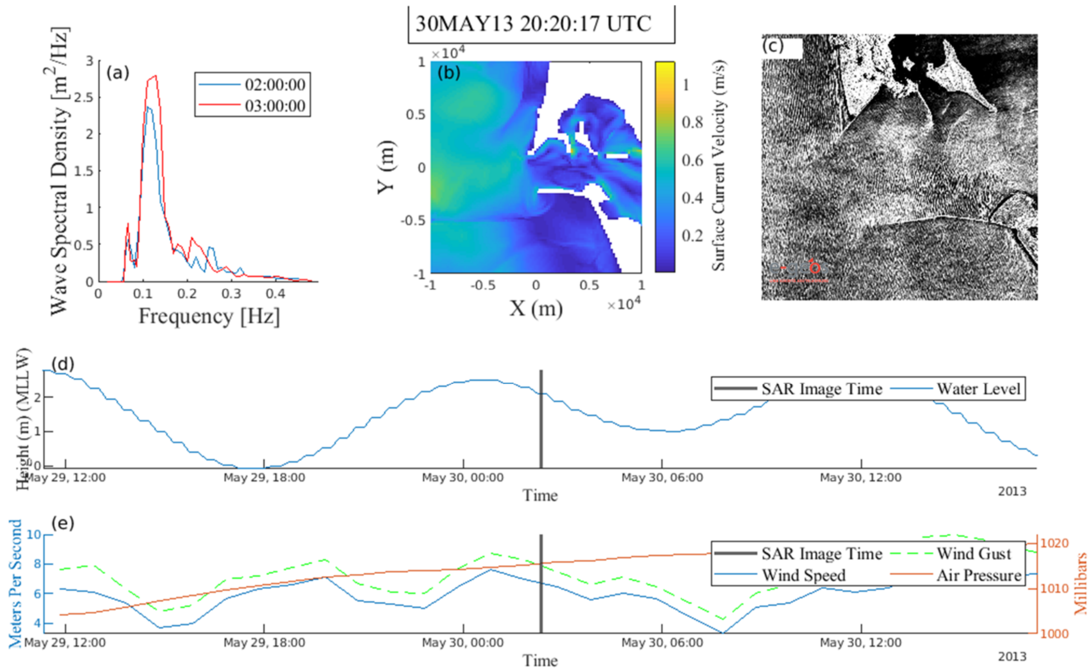

Figure 5: Environmental Conditions for 30 MAY 2013 02:26:20 UTC SAR image including (a) NOAA buoy 46029 energy spectrum (b) ROMS generated surface currents (c) SAR image (d) ROMS generated water level for MCR (e) Wind speed and Air Pressure from NOAA buoy 46029

2.4.4. June 8, 2013 02:14:14 UTC

The June 08, 2013 02:14:14 UTC image was collected during a slack tide just prior to a flood tide. Mild currents are predicted with a velocity range between the jetties of 1 to 1.5 m/s. The energy spectrum from the buoy shows a bimodal spectrum at both the 2:00 UTC and 3:00 UTC measurements. The spectrum has a low frequency peak of 0.0525 Hz and a higher frequency peak of 0.12 Hz. Air pressure is falling, and wind speeds are constant during the SAR image capture time.

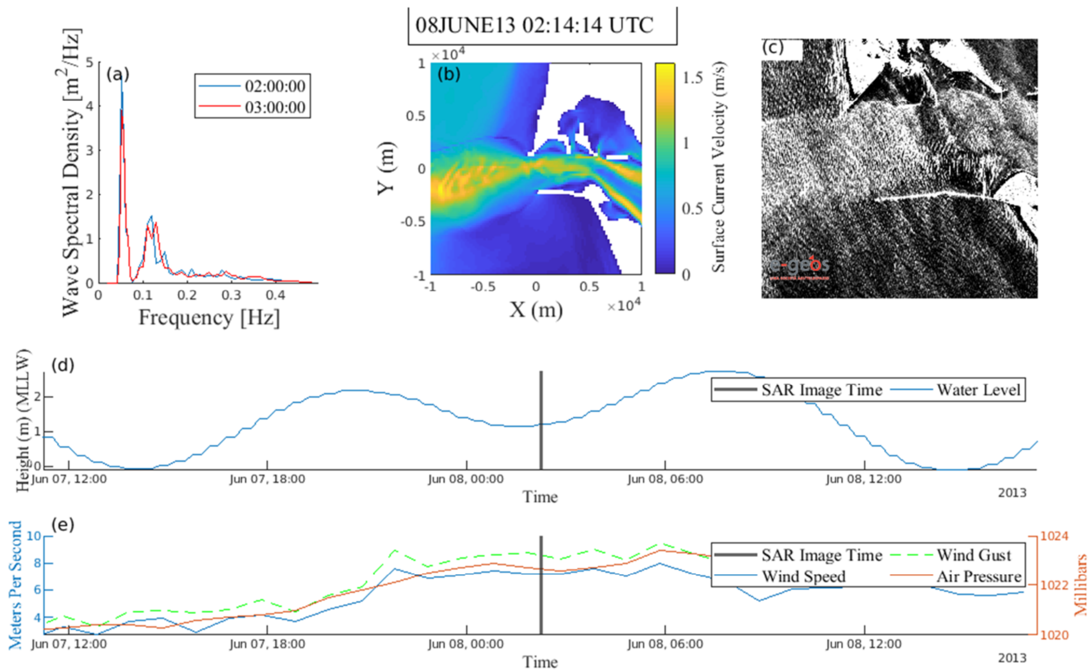

Figure 6: Environmental Conditions for 08 JUNE 2013 02:26:20 UTC SAR image including (a) NOAA buoy 46029 energy spectrum (b) ROMS generated surface currents (c) SAR image (d) ROMS generated water level for MCR (e) Wind speed and Air Pressure from NOAA buoy 46029

2.5. Bathymetry Inversion

A methodology for data assimilation and bathymetric inversion in a nearshore environment was described by Wilson et al. (2010) and is the basis of the methodology presented here. Wilson et al. (2010) implemented a weighted least squares method with Bayesian estimation using in situ observations of wave height and alongshore current to generate bathymetric estimates. Their methodology relied on an ensemble consisting of 150 realizations of bathymetry and providing these realizations as input to the numerical models. The ensemble of model results was then used to calculate the covariance matrix between model variables at discrete locations and the other variables in the modeled fields. In contrast, the method of bathymetry inversion presented herein utilizes SAR generated wavenumber-frequency pairs without requiring an ensemble-based approach for estimating covariance.

To implement this approach, a prior bathymetry ($\bar{h}$), or initial estimate of bathymetry is required. This prior bathymetry can be a “best-guess,” derived from a basic knowledge of general inlet bathymetries. The purpose of this prior best-guess bathymetry is to linearize and regularize the inverse problem. In order to calculate a correction (Δh) at the N model points and update the prior estimate to produce a posterior bathymetry ($\tilde{\mathrm{h}}$), a cost function must be minimized using a weighted least squares approach. This cost function contains two components: the first component tries to make sure that the predicted wavenumbers ($\mathrm{k}(\tilde{\mathrm{h}})$) at the M observation points are as close to the SAR observed wavenumbers ($\mathrm{k_o}$) as possible, and the second component will try to ensure that Δh is a small correction. The weights of the two components materialize as W and $\mathrm{W_h}$ and are positive-definite weighting matrices as described in Wilson et al. (2010), $\mathrm{W} = \mathrm{C_o}^{-1}$ where $\mathrm{C_o}$ is an M x M observation error covariance matrix and $\mathrm{W_h} = \mathrm{C_h}^{-1}$ where $\mathrm{C_h}$ is a N x N prior bathymetry error covariance matrix. The observation error covariance matrix ($\mathrm{C_o}$) provides the covariance between observation errors at each observation point. The result is the following cost function, that when minimized produces the optimal posterior bathymetry estimate.

$$J_o[\Delta h] = \left(\frac{\partial k}{\partial h}\Delta h - \left(k_o - k(\bar{h})\right)\right)^T \cdot W \cdot \left(\frac{\partial k}{\partial h}\Delta h - \left(k_o - k(\bar{h})\right)\right) + \Delta h^T W_h \Delta h \qquad \textbf{(1)}$$

Note that in equation (1), $\mathrm{k}(\tilde{\mathrm{h}})$ is approximated by $\mathrm{k}(\bar{\mathrm{h}}) + \frac{\partial \mathrm{k}}{\partial \mathrm{h}}\Delta\mathrm{h}$. Δh is an N x 1 vector while $\mathrm{k}(\bar{\mathrm{h}})$ and $\mathrm{k_o}$ are M x 1 vectors. $\frac{\partial \mathrm{k}}{\partial \mathrm{h}}$ is an M x N Jacobian matrix of the sensitivity of observed wavenumbers at the M observation locations to depth perturbations about the prior depth estimate at the N model points. The change in bathymetric depth, Δh, that minimizes the cost function in equation (1) is, (e.g., Evensen, 2007)

$$\Delta h = C_h \left(\frac{\partial k}{\partial h}\right)^T \left(\left(\frac{\partial k}{\partial h}\right) C_h \left(\frac{\partial k}{\partial h}\right)^T + C_o\right)^{-1} \left(k(\bar{h}) - k_o\right) \qquad \textbf{(2)}$$

In equation (2), $\frac{\partial \mathrm{k}}{\partial \mathrm{h}}$ is generated by differentiating the linear dispersion relationship including currents with respect to depth and solving for $\frac{\partial \mathrm{k}}{\partial \mathrm{h}}$; the dependence of currents and wave angle on depth are neglected in the calculation of $\frac{\partial \mathrm{k}}{\partial \mathrm{h}}$, as an approximation. The covariance matrices described with this method follow a Gaussian parametric form

$$C = \sigma^2 exp\left(\frac{-\left(x_i - x_j\right)^2}{2{L_x}^2} - \frac{\left(y_i - y_j\right)^2}{2{L_y}^2}\right) \qquad \textbf{(3)}$$

where x and y are the coordinates of observation or model points. L_x, and L_y are length scales for the respective coordinates and σ is the amplitude of vertical variance for the error of the prior bathymetry.

2.5.1. Computation of Covariance Matrices in Observational Domain

Computing covariance matrices for the model domain has limitations due to the large number of model points and subsequent large covariance matrices. To increase computational efficiency and reduce storage requirements, we can interpolate the N model points to the M observation point grid, thereby simplifying the multiplication of covariance matrices. For this derivation we will redefine $\frac{\partial \mathrm{k}}{\partial \mathrm{h}} = \Gamma$, and then identify two terms from equation (2) that will be simplified. $C_h(\Gamma)^T$ will be identified as term 1 and $(\Gamma)C_h(\Gamma)^T$ will be term 2. We are able to recognize that Γ in observational space (Γ_o) is a diagonal matrix; this is because we are assuming a slowly varying bathymetry and therefore the dispersion relationship is a local condition. Any variations in depth will only impact the wavenumber at that same observation point because there is no sensitivity to any other location. Therefore, to specify the covariance matrix in observational space we need only define a vector $\hat{\Gamma} = \frac{\partial k}{\partial h}$

corresponding to the sensitivity at the observation points, and then $\Gamma_o = diag[\widehat{\Gamma}]$ where Γ_o is an M x M diagonal matrix. With the model points interpolated on the observational grid and using the Gaussian parametric form shown in equation (3) it is possible to then calculate the covariance matrix between the depth at the observation points and the depth at the model grid points (C_{oh}). With that definition, term 1 evaluated in observational space can be written as follows:

$$C_h\, \Gamma^T = {C_{oh}}^T diag(\hat{\Gamma}) \tag{4}$$

A similar simplification can be applied to term 2 of equation (2), by defining C_{oo} as an M x M covariance matrix between the depths at the observation points; it is calculated using the same Gaussian parametric form as equation (3). Term 2 can then be written as

$$\Gamma C_h\, \Gamma^T = diag(\hat{\Gamma}) C_{oo} diag(\hat{\Gamma}) \tag{5}$$

The simplified terms can now be substituted back into equations (2), and the final equation for the updated bathymetry estimate is as follows:

$$h = \bar{h} + {C_{oh}}^T diag(\hat{\Gamma})\left(diag(\hat{\Gamma}) C_{oo} diag(\hat{\Gamma}) + C_o\right)^{-1}\left(k(\bar{h}) - k_o\right) \tag{6}$$

The MATLAB code using the bathymetry inversion discussed above can be found in Appendix A.

2.6. Wave Direction Filtering

It is common for the MCR to experience swells arriving from both the northwest and southwest. Such bidirectional conditions were sometimes present in the SAR observations; these conditions are clearly seen in the May 21st image. The wave directions observed by the SAR can be determined by finding the direction of the kx/ky vector and relating it to the sensor look direction and how the look direction relates to true north. As we will see in Figure 8, the observations can clearly be grouped by direction.

An observed wavenumber now has a known wave direction but still will need to be associated with a frequency in order to be useful for the assimilation procedure. The directional energy spectrum produced by the NOAA buoy can be utilized to gain an understanding of the frequency associated with each directional wave component. The directional spectrum therefore allows us to assign a frequency to a directional component of the waves arriving at the MCR. The SAR and NOAA buoy are observing the same waves and we can use wave direction to relate the SAR observed wavenumber and the NOAA buoy observed relative angular frequencies. Therefore, the results of this wave direction filtering process can be seen in Figure 7 & 8, and the process will be shown for the May 21st image. A SNR threshold of 10 was used for all observations in the wave direction filtering to reduce the amount of low quality points being assimilated.

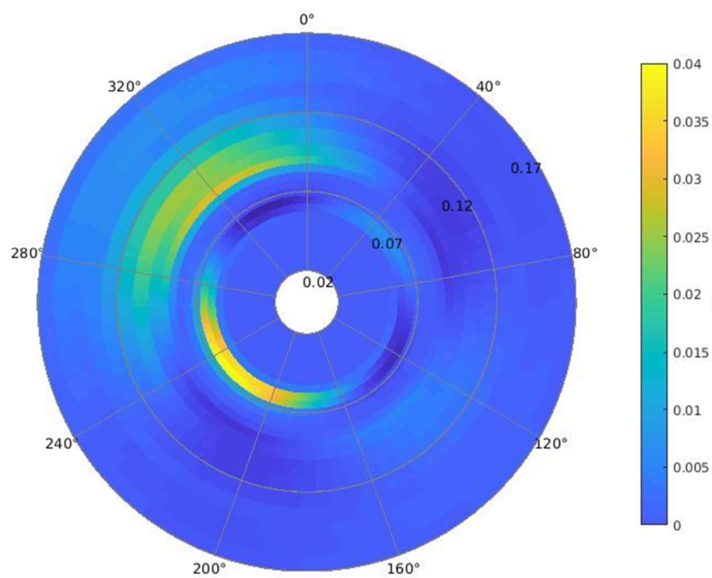

Figure 7: NOAA Buoy 46029 Directional Spectrum 21 MAY 2013 14:00 UTC, Directional peaks shown for the wave components arriving from the NW and SW

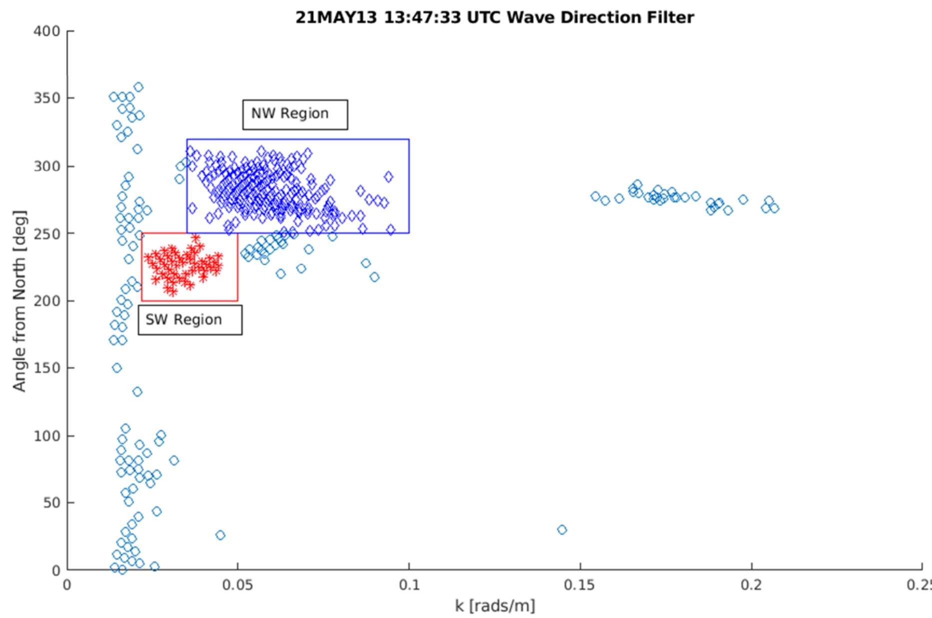

Figure 8: Wave Direction Filtering of SAR Observations 21 May 2013 13:47:33 UTC

The May 21st image was the image best suited for the wave direction filter as it had a bimodal spectrum and two distinct wave components- one arriving from the southwest and the other from the northwest. The crisscross wave pattern from these two wave trains arriving from opposing directions can clearly be seen in the SAR image. These wave components can be seen in the wavenumber observations when they are plotted with respect to wave direction. The lower wavenumber cluster shown in red in Figure 8 is associated with waves arriving from the southwest with a peak frequency of 0.0625 Hz. This frequency corresponds to the spectral peak located from 189˚ to 265˚ in the directional spectrum shown in Figure 7. The higher wavenumber group shown in blue corresponds to the wave group arriving from the northwest with a frequency of 0.1 Hz. Again, this can be confirmed by the spectral peak arriving from 280˚ to 340˚ in Figure 7.

2.6.1. General Application of Wave Direction Filter

To apply the wave direction filter to additional SAR images, we will set a few criteria based on the results of the wave direction filtering of the May 21st image. SAR observations will be clustered into two distinct regions; designated as the northwest and southwest regions. The northwest region is associated with observations that arrive from 250˚ to 320˚ and have a wavenumber between 0.035 and 0.1 rad/m. This region captures observations of wave components arriving at the MCR from northwest. Observations in this region can be seen for all the images analyzed in this study. The southwest region includes observations arriving from 200˚ to 250˚ that have a wavenumber in the range of 0.022 to 0.05 rad/m. Occasionally there is energy observed in the southwest region, most prevalently in the May 21st and June 8th observations. The longer waves associated with the southwest region are often generated by a coastal jet that extends along the Oregon coast (Ellenson & Özkan-Haller, 2018). It should be acknowledged that the observations with very low wavenumbers (<0.02 rad/m) that follow the scalloped pattern were determined to be low quality data and were not assimilated in the inversion. These data points had low SNR and would have wavelengths beyond those of interest here. To retain the highest quality and most realistic observations, all data outside of the northwest and southwest regions was disregarded.

When applying the wave direction filter regions to other SAR images there was a discernible division of the observation in the northwest region. When the location of each cluster of wavenumber observations in the region is explored, as shown in Figure 9 for the June 8th image, it is visible that data points in the lower portion of the northwest region are located south of the south jetty. We recognize that the two separate clusters of observations in the northwest cluster are actually the same wave components. The reason for the separation between the two clusters is due to refraction around the south jetty. The division of the wavenumber observations arriving from the northwest was a common occurrence in additional SAR images. When a frequency is being assigned to each cluster of wavenumber observations, it is important to recognize that the wave components arriving from the northwest should be assigned a single frequency as a group.

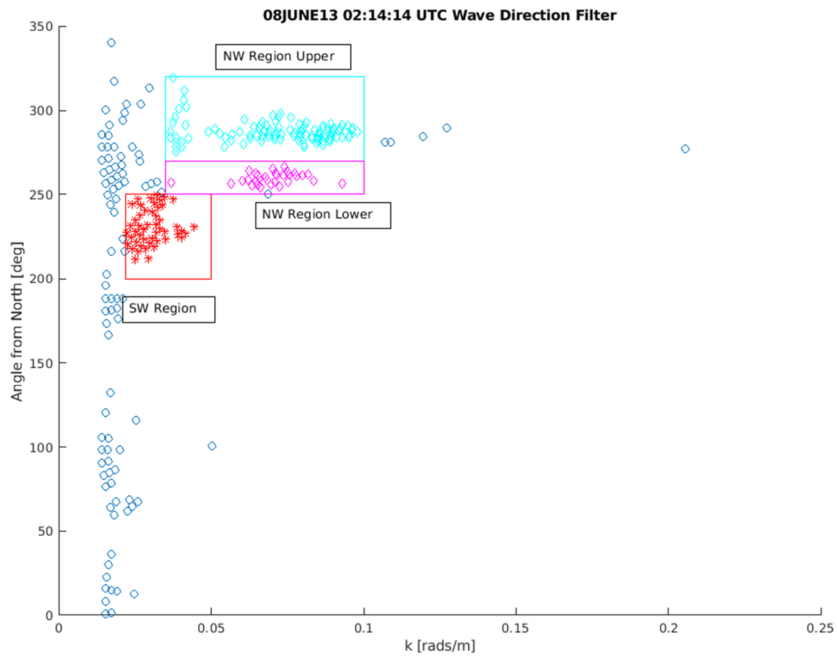

Figure 9: Wave Direction Filtering of SAR Observations 08 June 2013 02:14:14 UTC

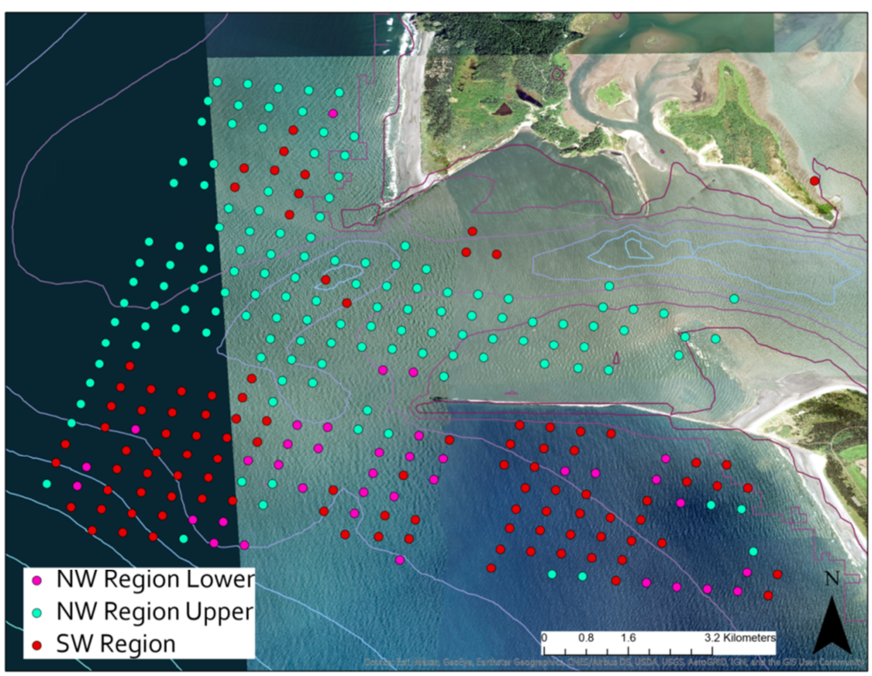

Figure 10: Location of SAR observations, cyan is upper NW region, magenta is the lower NW region cluster, and red is the SW region cluster

Chapter 3: Results

In this section we discuss the results of inversions completed with SAR Observations. We will review the results through both a qualitative and quantitative lens to provide an insight to how the method is estimating the larger scale bathymetric patterns as well as the smaller, more minute features. For a qualitative analysis, we will visually review the posterior bathymetry and comment on how the method has predicted the larger features; ODMDS A & B, the navigational channel, Clatsop Spit, and Peacock Spit. Overall patterns of underestimation or overestimation of depth will also be discussed.

To quantify the performance of the bathymetry estimation we will use root-mean-square error (RMSE) and bias across three transects, as well as the location and depth of the MCR navigational channel along a transect. The three transects were selected to provide a detailed view of the estimated bathymetry and how the prior bathymetry was updated with respect to the key features. Transect A-A, B-B, and C-C can be seen in Figure 12 and have the following characteristics; A-A follows the MCR navigational channel alignment as it crosses the domain, B-B is a north-south transect seaward of the jetties that intersects Peacock Spit before arcing south and crossing the navigational channel, and C-C is a north-south transect that begins at the shoreward end of the north jetty then crosses the navigational channel and Clatsop Spit and terminates at the south jetty. Transect C-C provides comparison of the depth and shape of the navigational channel for the estimated bathymetries.

3.1. Verification with Model-Derived Data

Prior to assimilating the SAR observations, model-derived data was assimilated to evaluate the skill of the inversion method as well as to set a baseline for performance. Model-derived data consisted of calculated output fields sampled at locations consistent with SAR observations. In our case, the COAWST model was run using the true bathymetry as an input, to provide the surface wave properties required for assimilations. The model-calculated fields were sampled using the SAR observation locations and grid spacing. The observation values were calculated by interpolating the velocity components, wave direction, and true depth at the SAR observation locations. The dispersion relationship including current influences was used to solve for wavenumber using the interpolated data and the wave frequency as observed by NOAA buoy 46029. An assumption is being made that the model-derived observations are associated with only a single component that corresponds with the NOAA buoy frequency.

Currents and wave direction from the prior bathymetry model were used for the inversion, as is standard for all the completed inversions discussed herein. The inversion results using the model-derived data showed that the model had skill and could accurately correct the prior bathymetry to generate features; specifically the navigational channel, Peacock Spit, Clatsop Spit, and ODMDS A. These results can be seen in Figures 11 & 12. Depth estimations at Peacock Spit were underestimated and created a bathymetry that is shallower than the true depth (see Figure 12e). It should be noted that there is limited spatial coverage of observation points to assimilate in the area of Peacock Spit and therefore the posterior bathymetry did not show significant improvement in the northern portion ($x > 4{,}000$ m) of transect B-B in Figure 12e. The inversion method accurately locates the navigational channel, as can be seen in the alongshore transects in Figures 12e & 12f; however, the method underestimates the true depth of the channel. The extent and shape of Clatsop Spit is well-estimated by the model; the depth however, is underestimated when compared with the true bathymetry (see Figure 12f). Completing the assimilation and inversion using model-derived data not only provides a baseline, but it also shows the best performance that high quality observations, a highly-skilled model, and ample spatial coverage can produce.

Table 1: Root-mean-square error (m) for the depth at transects for assimilation using model-derived observations

RMSE for Inversion Using Model-Derived Data													
Assimilation	Domain RMSE [m]	Transect RMSE [m]			Transect Bias [m]			Mean Transect Depth [m]			Mean Percent Error (%)		
		A-A	B-B	C-C	A-A	B-B	C-C	A-A	B-B	C-C	A-A	B-B	C-C
Prior	1.96	7.66	3.12	4.25	-3.89	0.52	1.80	22.56	16.89	10.41	33.94	18.49	40.83
21 MAY 13 13:47:33 UTC	**1.60**	**4.19**	**1.71**	**3.56**	-3.25	-0.25	-2.70				**18.59**	**10.11**	**34.21**
29 MAY 13 02:26:20 UTC	1.96	**4.83**	**2.66**	**1.20**	-3.07	0.77	-0.78				**21.43**	**15.76**	**11.53**
30 MAY 13 02:20:17 UTC	2.21	**2.99**	**1.89**	**2.05**	-1.94	0.93	-0.97				**13.26**	**11.18**	**19.69**
08 JUNE 13 02:14:14 UTC	**1.57**	**3.93**	**1.11**	**2.01**	-3.02	-0.34	-1.49				**17.41**	**6.55**	**19.34**

The RMSE for the inversion using model-derived data across the benchmark transects is shown in Table 1. Values that are an improvement over the prior bathymetry are highlighted in red. The domain RMSE describes the performance of the inversion across the entire area in which the observations were assimilated. The RMSE across the three-analysis transects provides a more detailed view of the model's performance and how the particular features were estimated. The RMSE across all three transects was improved for all of the four assimilations when compared to the prior bathymetry. The root-mean-square error relative to the average transect depth (RRMSE) also decreased, with all of the assimilations showing a reduction. The transect bias shows that in general the estimate bathymetries are shallower than the true bathymetry. In Figure 12f we can see that the posterior bathymetry is underestimated in the area of the navigational channel as well as Clatsop Spit. The most improvement can be seen in transect A-A where the minimum RMSE improvement was almost 2.8 meters and the maximum was nearly 4.7 meters. The root-mean-square-error relative to the average transect depth (RRMSE) further shows a 12% to 20% improvement for transect A-A when assimilating the model-derived observations. Transect B-B had a minimum RMSE improvement of 0.5 meters (May 29th) and a maximum improvement of 2.0 meters (June 8th) for the four assimilations. Transect C-C had a minimum RMSE improvement of 0.7 meters (May

21st) and a maximum improvement of 3.1 meters (May 29th) for the four assimilations.

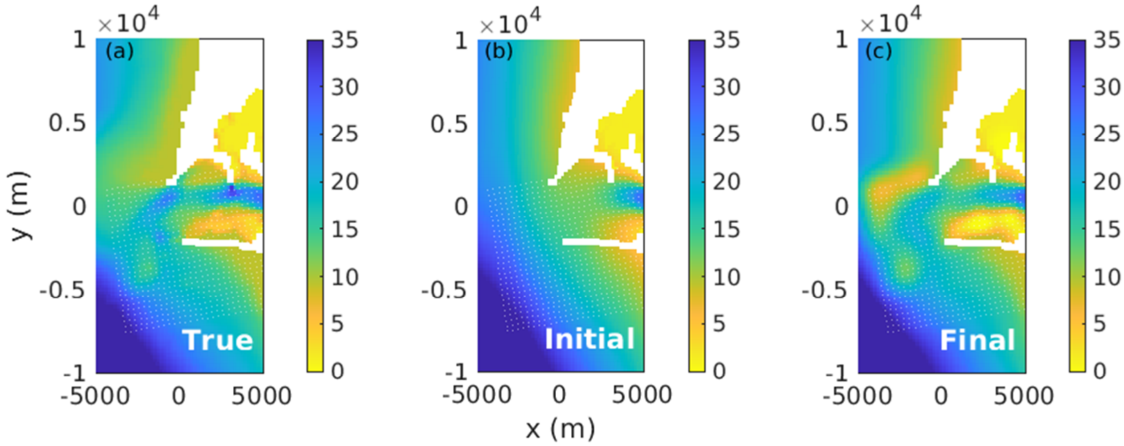

Figure 11: Results for assimilation using model-derived observations for 21 May 2013 13:47:33 UTC (a) true bathymetry (b) Prior "smoothed" bathymetry and (c) posterior “final” bathymetry

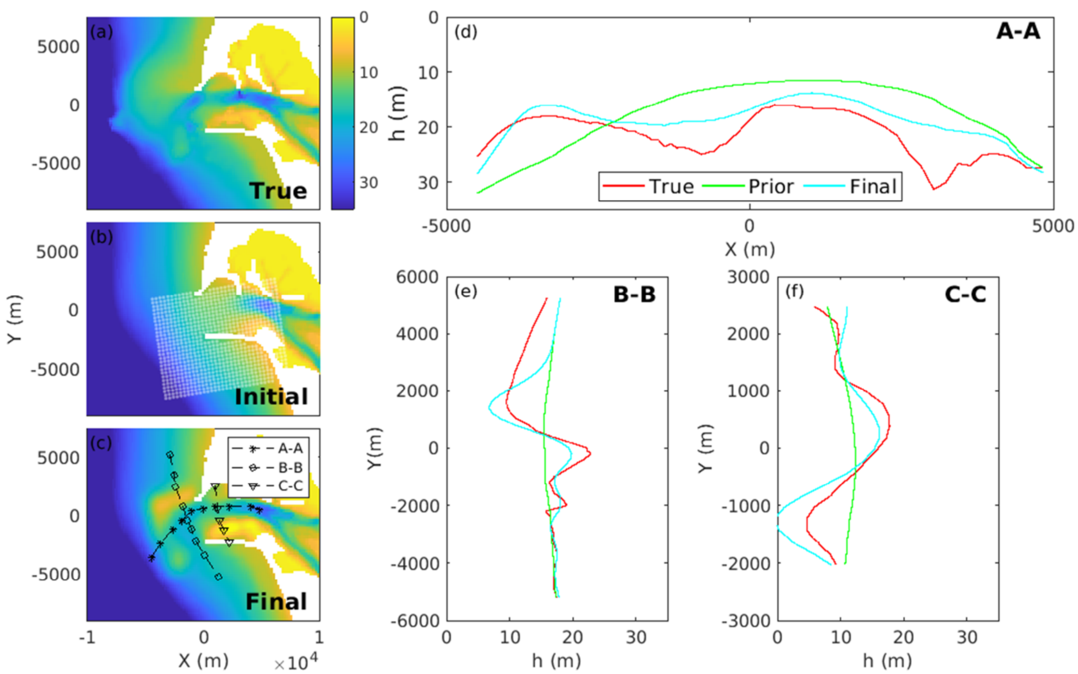

Figure 12: Results for assimilation using model-derived observations for 21 May 2013 13:47:33 UTC (a) true bathymetry (b) prior "smoothed" bathymetry and location of observations (c) posterior “final” bathymetry and transects used for analysis (d) transect A-A (e) transect B-B (f) transect C-C

3.2. Bathymetry estimates using SAR observations

In this section we will review the results of the assimilation using the wave direction filtering method and SAR observed wavenumbers for the following images: May 21, 2013 13:47:33 UTC, May 29, 2013 02:26:20 UTC, May 30, 2013 02:26:20 UTC, and June 08, 2013 02:14:14 UTC. We will first explore the root-mean-square error and bias across the three transects for each assimilation result as presented in Table 2. Secondly we will qualitatively compare the results of the assimilation versus the prior "smoothed" bathymetry. Included in this qualitative comparison will be a review of the SAR observations selected through the wave direction filtering process for assimilation. Reviewing the observational input alongside the assimilation results provides a chance to recognize patterns in the quality of results due to spatial coverage of observations. The assimilations will be reviewed and we will comment on where the method performed well and where it did not.

Table 2: Root-mean-square-error and bias for MCR transects A-A, B-B, C-C after assimilation SAR wavenumber observations

RMSE for Inversion Using SAR Observations													
Assimilation	Domain RMSE [m]	Transect RMSE [m]			Transect Bias [m]			Mean Transect Depth [m]			Mean Percent Error		
		A-A	B-B	C-C	A-A	B-B	C-C	A-A	B-B	C-C	A-A	B-B	C-C
Prior	1.96	7.66	3.12	4.25	-3.89	0.52	1.80	22.56	16.89	10.41	33.94	18.49	40.83
21 MAY 13 13:47:33 UTC	2.08	7.83	4.13	**2.66**	-3.89	0.79	1.93				34.69	24.48	**25.54**
29 MAY 13 02:26:20 UTC	2.82	**6.94**	5.78	8.21	0.92	3.51	6.83				**30.78**	34.24	78.84
30 MAY 13 02:20:17 UTC	3.01	12.63	4.44	**1.94**	-4.80	2.30	0.58				55.97	26.29	**18.62**
08 JUNE 13 02:14:14 UTC	2.66	**6.05**	5.87	9.57	-5.06	-0.46	5.36				**26.81**	34.76	91.94

Overall the quantitative results using the wave direction filtering method to assimilate SAR observations are mixed. In this section we will compare the overall domain RMSE, individual transect RMSE, and the RRMSE of the four assimilations against the baseline values of the prior bathymetry. In Table 2, values that are an improvement over the prior bathymetry are highlighted in red. With respect to the overall domain RMSE, none of the four assimilations produced a domain RMSE that was an improvement over the prior bathymetry. The May 21st assimilation had a slight increase in RRMSE in transects A-A & B-B from 33.94% to 34.69% and 18.49% to 24.48%, respectively. However, the RRMSE in transect C-C was improved by approximately 15%. The bias increased in the May 21st inversion for transects B-B and C-C, and A-A remained unchanged. Transect bias using the SAR observation shows that most often the estimated bathymetry is deeper than the true bathymetry, this being in contrast to the assimilation of model-derived observations when the estimated bathymetry was often too shallow.

3.2.1. May 21, 2013 13:47:33 UTC

The wave direction filtering method captures a good portion of wave energy in both the NW and SW regions. The associated frequencies as observed by the NOAA buoy for the clusters of SAR observations were 0.1 Hz for the NW region and 0.0625 Hz for the SW region. Observations showing refraction around the south jetty seem to be minimal; however it is possible that the cluster below the NW region boundary could be evidence of some refraction. Overall the filtering captured high quality data judging by the SNR (not shown); a filter with a higher threshold than the SNR of 10 used here may be able to reduce the selection of lower quality observations. Figure 13 shows a cluster of observations with corresponding wavenumbers greater than 0.15 that could be associated with a higher frequency peak; however these points were not assimilated as they were outside of the distinct wave direction filter regions.

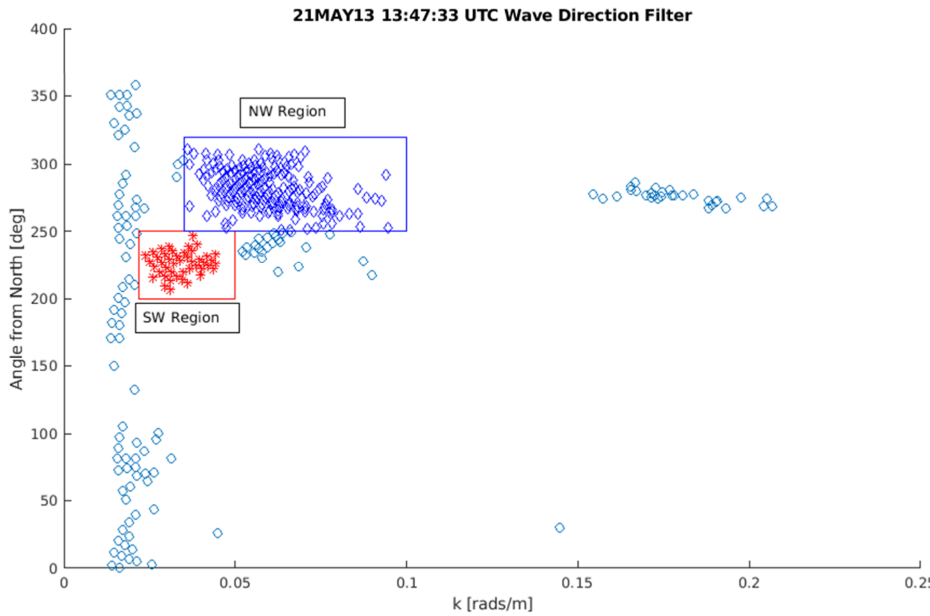

Figure 13: Wave direction filter for 21 MAY 2013 13:47:33 UTC showing the NW and SW regions for selecting observations to assimilate

The assimilation results for May 21st are shown in Figures 14 and 15. Figure 14 shows the overall domain in which the assimilation took place for the true bathymetry, prior bathymetry, and the posterior bathymetry. Figure 15 shows the three transects used for the quantitative analysis as well as the spatial coverage of the SAR observations. The posterior bathymetry when assimilating the May 21st SAR observations predicts multiple features present at the MCR including the navigational channel, Peacock Spit, and Clatsop Spit. The predictions include a continuation of the navigational channel from jetty A towards the tip of the north jetty; the location of the channel is shifted south when compared to the true bathymetry. This can also be seen in the large discrepancy in depth at the beginning of transect A-A in Figure 15d. This discrepancy in the depth is most likely responsible for a large portion of the RMSE calculated for transect A-A. Transect B-B in Figure 15e shows that the depth and location of the navigational channel are well estimated. The western extent of Clatsop Spit is well estimated by the posterior bathymetry, however the width of the spit as you trace transect C-C north to south is narrower than that seen in the true bathymetry. Due to limited spatial coverage of observations around Peacock Spit, it is poorly represented in the posterior bathymetry; however for the portion of Peacock

Spit where observations are available, the assimilation is attempting to reduce the depth. The portion of Peacock Spit that is overestimated in the northern extent of transect B-B (x = 2,000 m) was more closely examined and the overestimation was the result of a few low quality data points. A method to filter out these low quality observations could be beneficial in reducing the RMSE across the transect; however a method was not established for this study but could be an opportunity for future work.

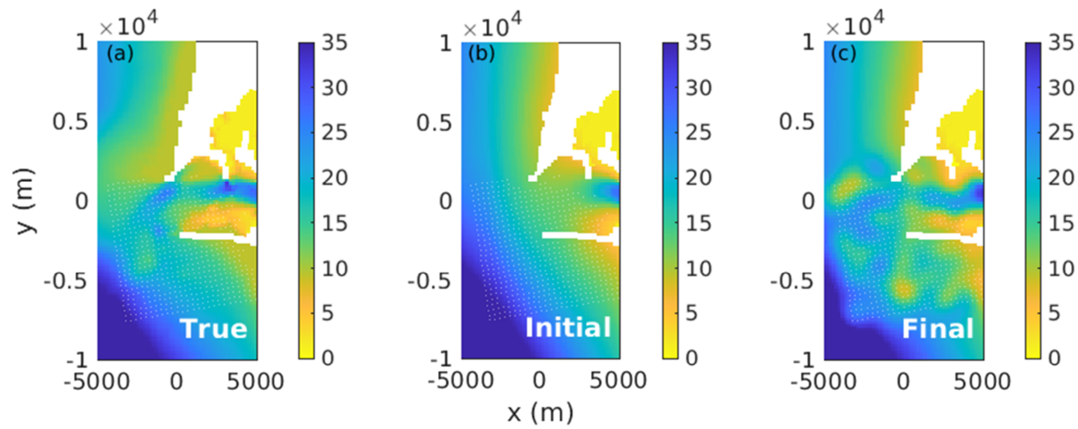

Figure 14: Results for assimilation using SAR observations for 21 May 2013 13:47:33 UTC (a) true bathymetry (b) Prior "smoothed" bathymetry and (c) posterior bathymetry

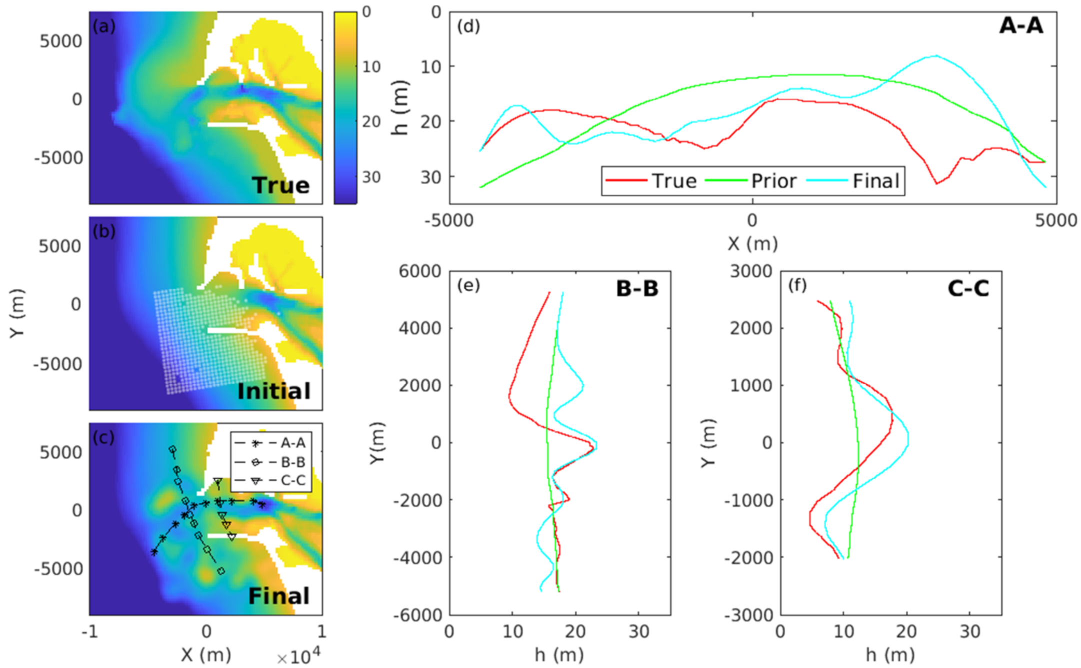

Figure 15: Results for assimilation using SAR observations for 21 May 2013 13:47:33 UTC (a) true bathymetry (b) Prior "smoothed" bathymetry and location of observations (c) posterior bathymetry and transects used for analysis (d) transect A-A (e) transect B-B (f) transect C-C

3.2.2 May 29, 2013 02:26:20 UTC

A large cluster of points were present in the NW region for the wave direction filtering of the May 29th observations and very few were included in the SW region as seen in Figure 16. Refraction of the wave component arriving from the northwest does not seem to be observed. Of note, there is a large amount of observation spread about the higher wave number range; greater than 0.1 rad/m. This image has the largest spread of observation with respect to wavenumber, when compared to the others. The frequencies associated with the NW & SW regions were 0.12 Hz and 0.0625 Hz respectively.

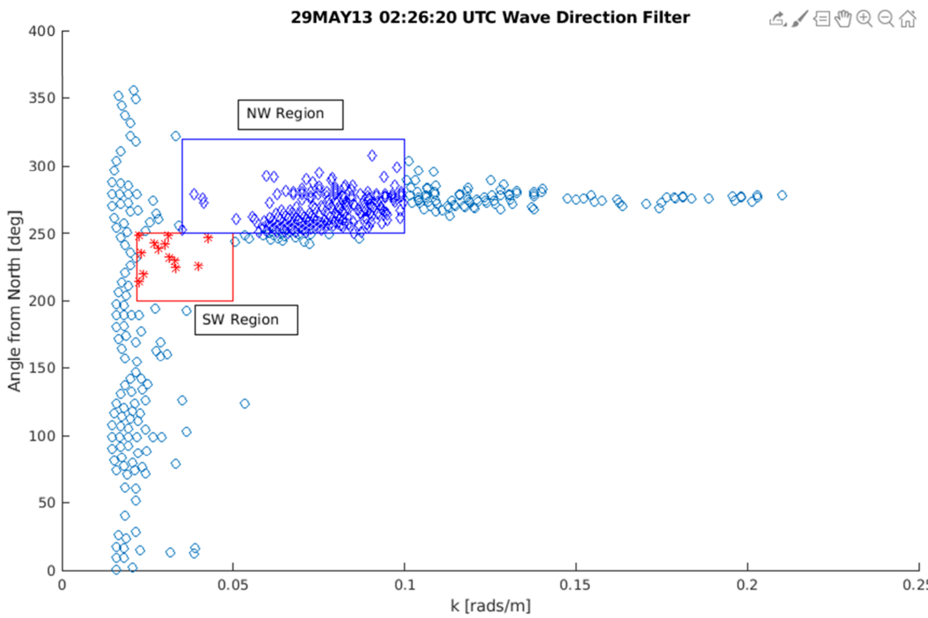

Figure 16: Wave direction filter for 29 MAY 2013 02:26:20 UTC showing the NW and SW regions for selecting observations to assimilate

The assimilation results for May 29st are shown in Figures 17 and 18. The overall posterior bathymetry for the assimilation that uses the May 29st SAR observations shows little resemblance to the true bathymetry. Transect A-A & B-B shown in Figure 15d & 15e allow us to see the overestimation of depth at the mouth of the inlet, however transect B-B shows that the overall shape of the navigational channel is well predicted. The posterior bathymetry along transect A-A, as shown in Figure 15d, indicates a good prediction of the depth for the eastern portion (x > 0 m) of the transect. May 29th has the second lowest RMSE for transect A-A. A large hole is predicted at the seaward end of the navigational channel that is not observed in the true bathymetry, looking at the spatial coverage of the observations we can see that there are few observations in the vicinity of this overestimated hole. Clatsop Spit is nearly nonexistent in the posterior bathymetry; however the assimilation did attempt to create Peacock Spit as can be seen in Transect B-B. The depth of Peacock Spit was overestimated at the northern extent of transect B-B, however the Spit was then underestimated in width.

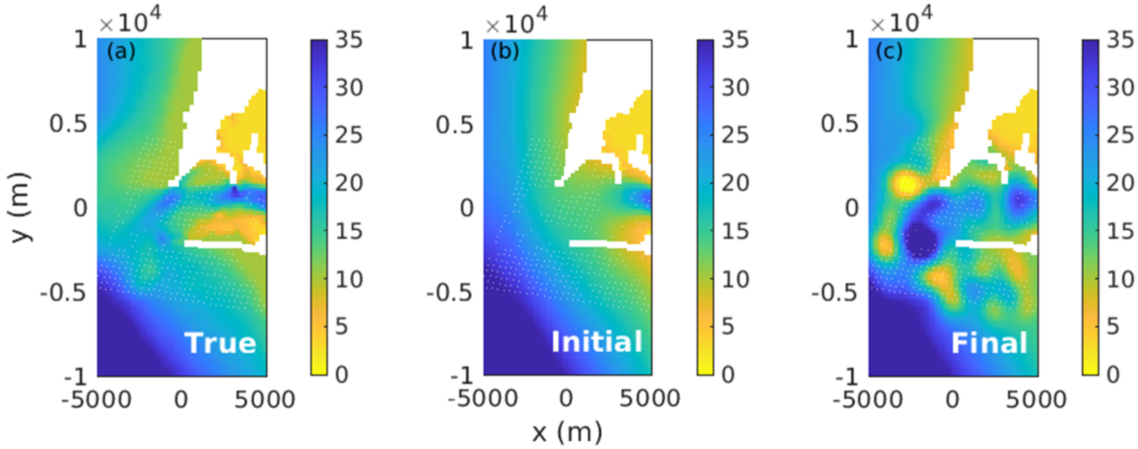

Figure 17: Results for assimilation using SAR observations for 29 MAY 2013 02:26:20 UTC (a) true bathymetry (b) Prior "smoothed" bathymetry and (c) posterior bathymetry

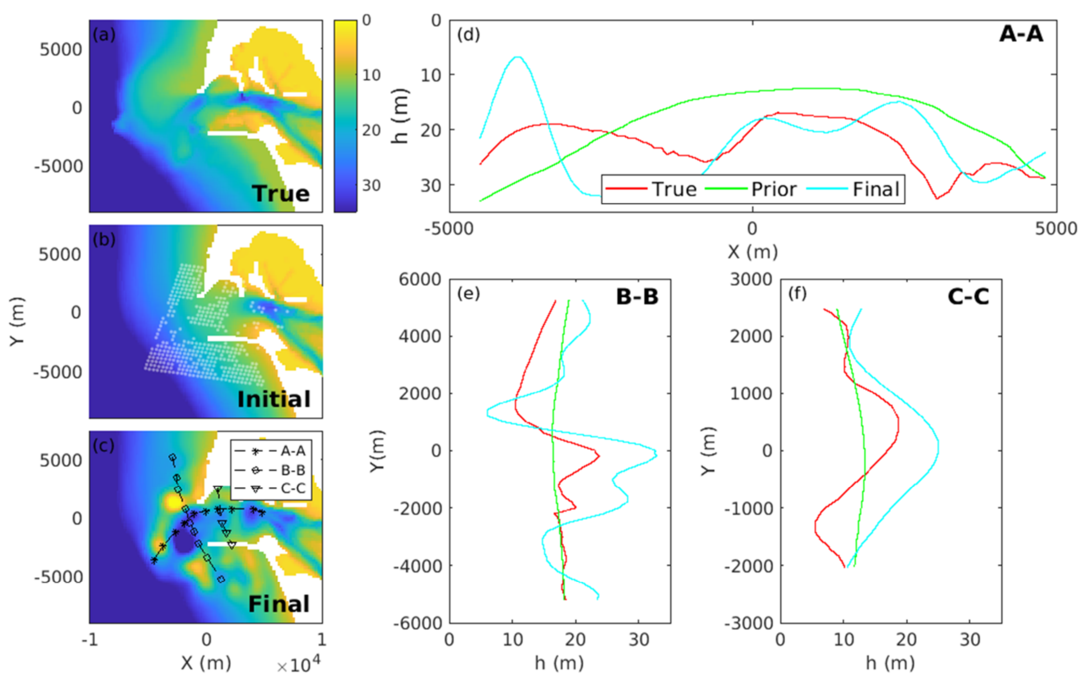

Figure 18: Results for assimilation using SAR observations for 29 MAY 2013 02:26:20 UTC (a) true bathymetry (b) Prior "smoothed" bathymetry and location of observations (c) posterior bathymetry and transects used for analysis (d) transect A-A (e) transect B-B (f) transect C-C

3.2.3 May 30, 2013 02:20:17 UTC

A large cluster of points were present in the NW region for the wave direction filtering of the May 30th observations and very few were included in the SW region as seen in Figure 19. Refraction of the wave component arriving from the northwest is present and the division of the cluster is clear in the NW region. There are generally few observations with wavenumber greater than 0.1 rad/m. The frequencies associated with the NW & SW regions were 0.115 Hz and 0.0675 Hz respectively.

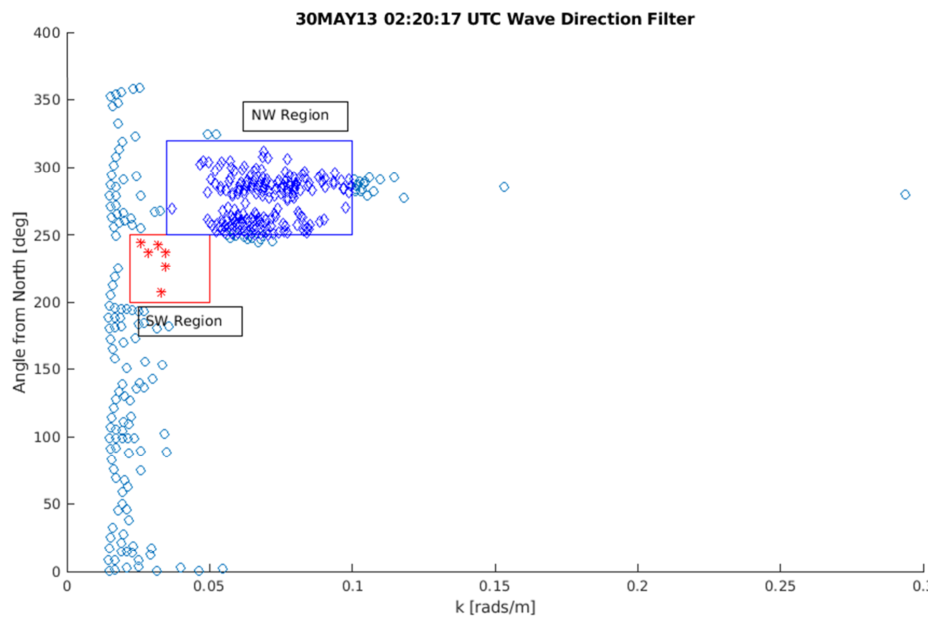

Figure 19: Wave direction filter for 30 MAY 2013 02:20:17 UTC showing the NW and SW regions for selecting observations to assimilate

The assimilation results for May 30st are shown in Figures 20 and 21. The posterior bathymetry when assimilating the May 30st SAR observations mostly varies from the prior bathymetry in the area near the tip of jetty A, Clatsop Spit, and northwest of the north jetty. The navigational channel is poorly represented in this assimilation. The navigational channel transect A-A does not show a lot of similarities between prior and posterior, most noticeably in the eastern portion of transect A-A, which is characterized by a very shallow region in the vicinity of Jetty A. A lack of observations along the navigational channel near the tip of Jetty A most likely led to the underestimation in this area. Clatsop Spit has correctly been estimated to extend parallel to the south jetty; the depth of the spit is well estimated as seen in Figure 21f. Peacock Spit is again overestimated in the northern extent of transect B-B and then underestimated closer to the navigational channel. The May 30th assimilation produced the best estimation of ODMDS A in both size and depth.

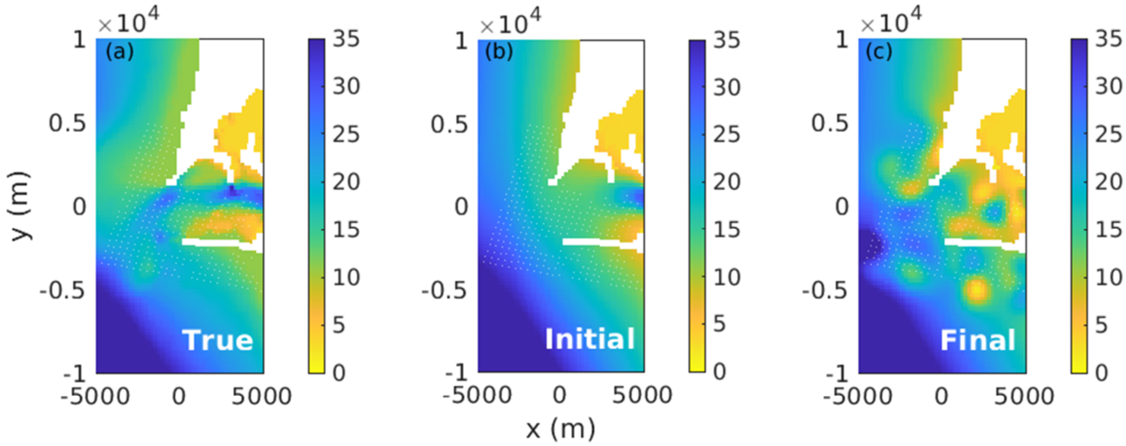

Figure 20: Results for assimilation using SAR observations for 30 MAY 2013 02:20:17 UTC (a) true bathymetry (b) Prior "smoothed" bathymetry and (c) posterior bathymetry

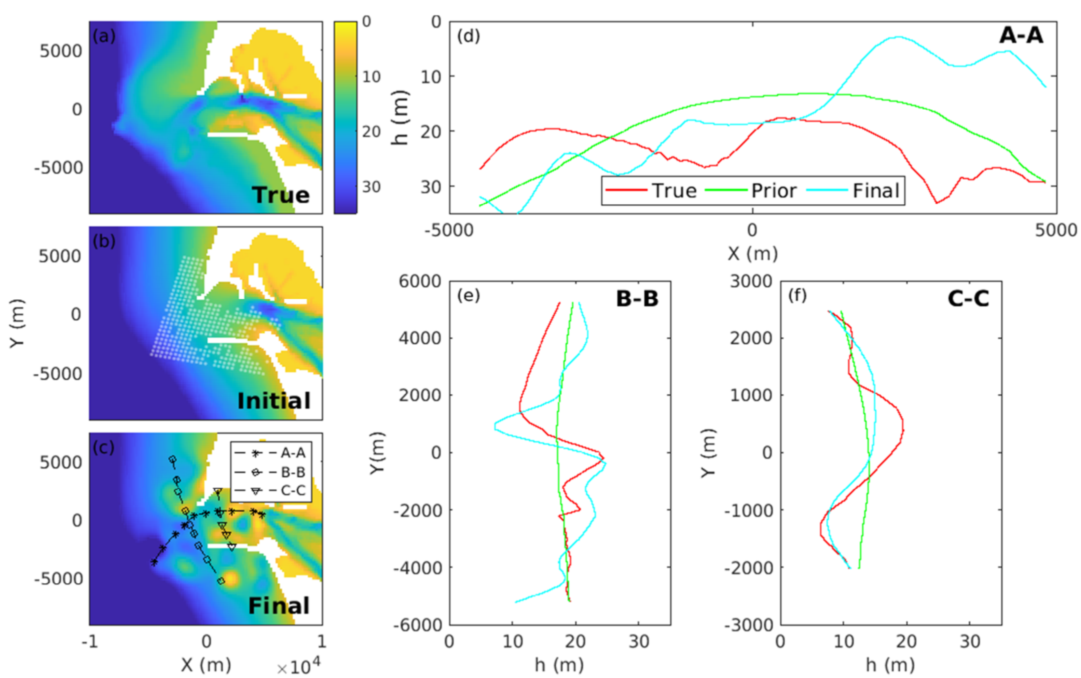

Figure 21: Results for assimilation using SAR observations for 30 MAY 2013 02:20:17 UTC (a) true bathymetry (b) Prior "smoothed" bathymetry and location of observations (c) posterior bathymetry and transects used for analysis (d) transect A-A (e) transect B-B (f) transect C-C

3.2.4 June 8, 2013 02:14:14 UTC

Figure 22 shows the wave direction filtering of the SAR Observations for June 8th, large clusters of observations were present in both the NW & SW regions. Refraction of the wave component arriving from the northwest is present and the division of the cluster is clear in the NW region. A third cluster is located in the NW region associated with observed wavenumbers less than 0.05 rad/m, this cluster is not observed in any of the other three images. A significant amount of observations are present in the SW region, similar to May 21st. Another point of interest in Figure 22 is the lack of observations with observed wavenumbers greater than 0.1 rad/m, this is in contrast to May 21st and May 29th. The frequencies associated with the NW & SW regions were 0.115 Hz and 0.0525 Hz respectively.

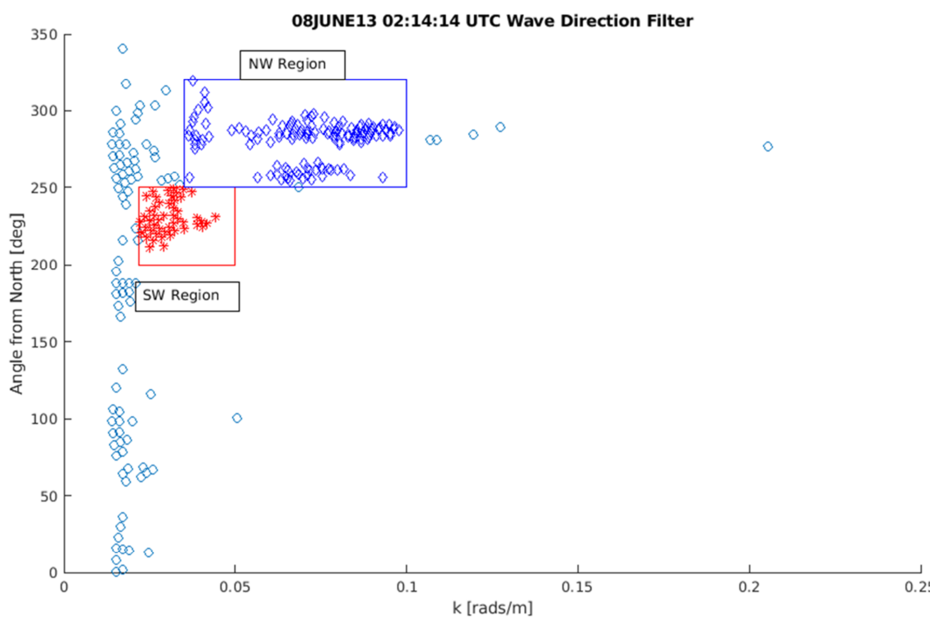

Figure 22: Wave direction filter for 08 JUNE 2013 02:14:14 UTC showing the NW and SW regions for selecting observations to assimilate

The assimilation results for June 8th are shown in Figures 23 and 24. For the June 8th assimilation transect A-A in Figure 24d shows that the posterior transect has a similar shape to that of the true bathymetry, however the depth of the posterior is underestimated for a majority of the transect. We can also see that the center of the navigational channel is roughly estimated in transect C-C shown in Figure 24e, the depth however is over estimated and the location is shifted to the south. Clatsop spit in the posterior bathymetry is estimated to be approximately five meters shallower than that of the true bathymetry, the north-south extent of spit is underestimated and reduced from that of the prior bathymetry. For this assimilation the spatial coverage of the observation points over Peacock Spit is good, however the assimilation produces many holes and shoals that are not consistent with the true bathymetry. This is confirmed in transect B-B which shows little resemblance to the true bathymetry along the northern extent of transect B-B. ODMDS A is estimated for the June 8th image; however it is connected to the bar like feature running north-south in front of the inlet.

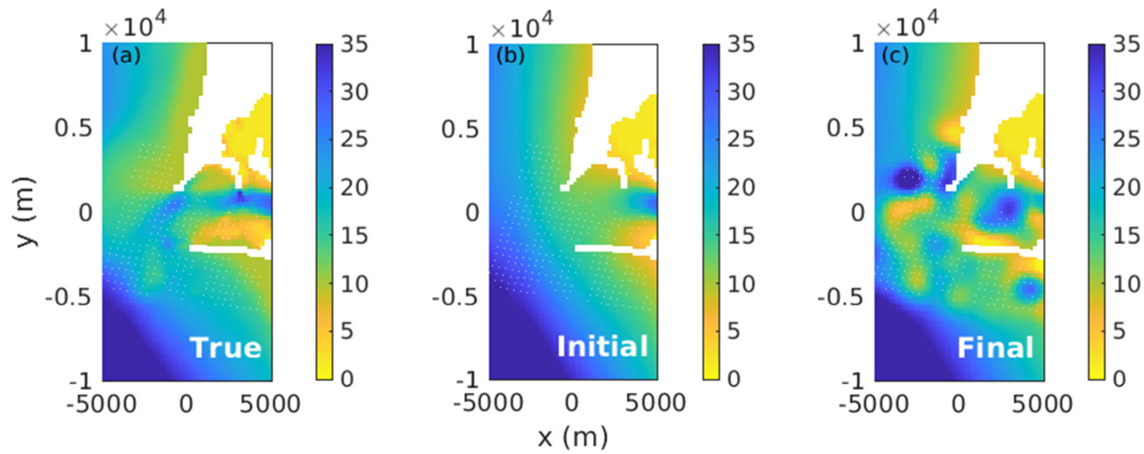

Figure 23: Results for assimilation using SAR observations for 08 JUNE 2013 02:14:14 UTC (a) true bathymetry (b) Prior "smoothed" bathymetry and (c) posterior bathymetry

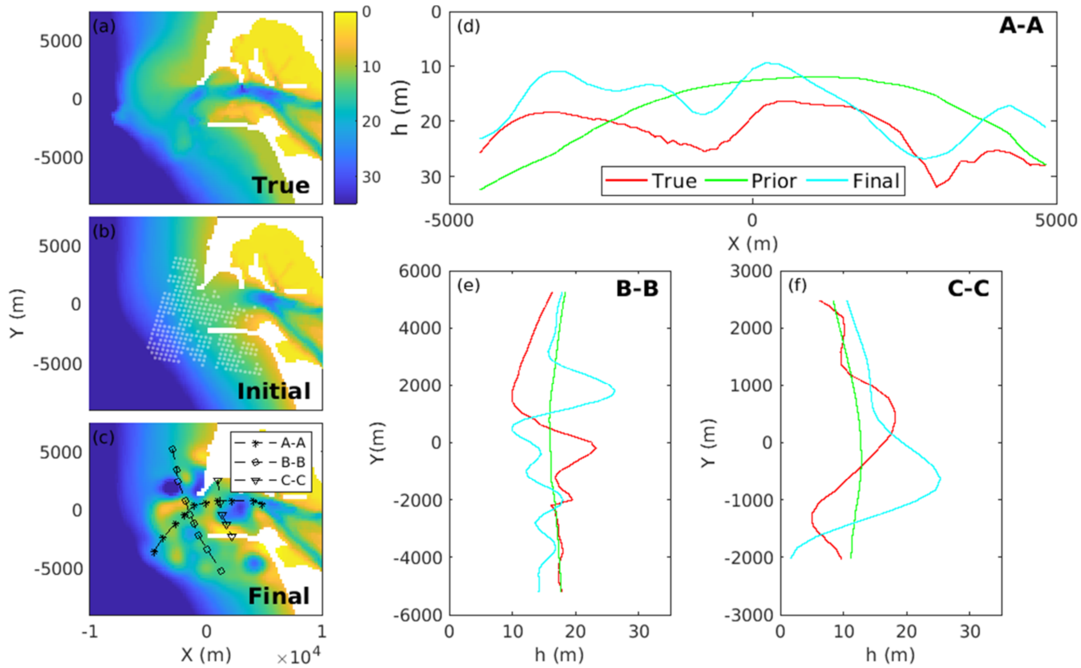

Figure 24: Results for assimilation using SAR observations for 08 JUNE 2013 02:14:14 UTC (a) true bathymetry (b) Prior "smoothed" bathymetry and location of observations (c) posterior bathymetry and transects used for analysis (d) transect A-A (e) transect B-B (f) transect C-C

Chapter 4: Discussion

4.1. Sensitivity to Assigned Frequency for Each Observation

The largest uncertainty of this method is assigning a frequency to a wavenumber observation. In this section we will explore how this uncertainty manifests itself in the results. Earlier, we used model-derived data to verify the method's skill and saw the detailed bathymetry that could be estimated using so called "perfect" or model-derived observations. We will be developing a different kind of twin experiment, where we will assemble a very specific hybrid data set to help us understand the manifestation of frequency uncertainty in the inversion. This data set is termed "hybrid" because it is using a combination of the SAR observations and model generated fields. The model-derived data set discussed in section 3.1 was constructed by using a single frequency and calculating a wavenumber using model outputs. In contrast, the hybrid data set discussed here was fashioned by using the SAR observed wavenumber, SAR observed wave directions, the true depth at the observation point, and model generated currents over the true bathymetry. Using the dispersion relationship with currents and the previously mentioned inputs, we can calculate the relative angular frequency that corresponds to the known true depth at the observations points. To remove the uncertainty from limited spatial coverage of observations, all observation points were used in this assimilation. The SAR wavenumber observations with the largest SNR at each observation point were selected. The calculated "true" frequency can then be linked to the SAR observations and the assimilation can be completed.

Figure 25 shows the calculated frequencies for the model-observation hybrid data; we can see the reference line on the y-axis for the frequencies of 0.0625 Hz and 0.1 Hz selected from the energy spectrum for the wave direction filtering method. The cluster of frequencies in Figure 25 clearly resembles those of NW and SW regions in the wave direction filtering method. The frequencies selected for the wave direction filter look to be an average value for the clusters of calculate true frequencies, therefore showing that the select frequencies are a good representation of the true frequencies.

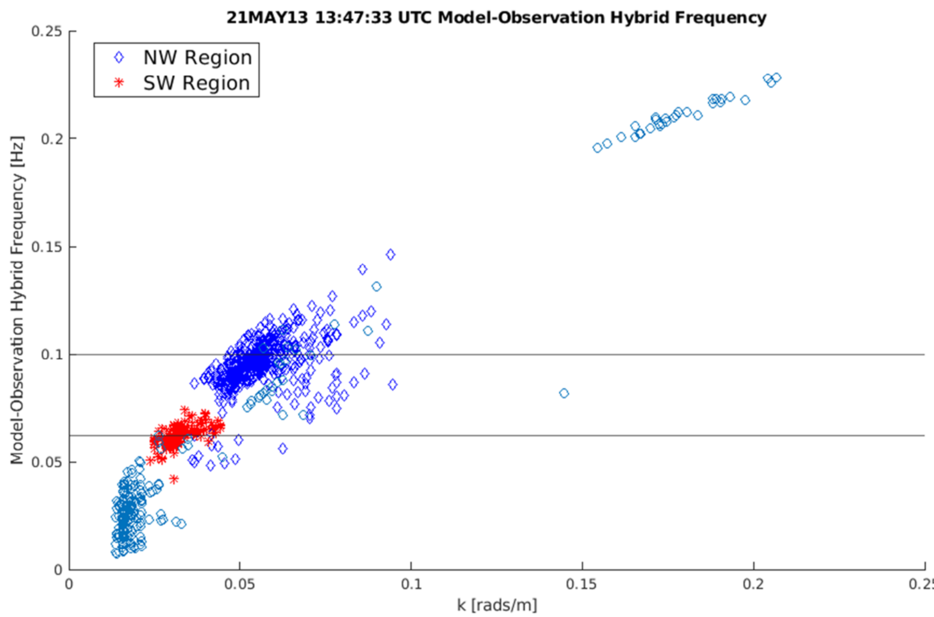

Figure 25: Model-Observation hybrid frequencies calculated using SAR observed wave direction and wave direction, true depth, and model generated currents; the reference lines on the y-axis are associated with the spectral peak frequencies used for the observations selected by the wave direction filtering process

This exercise was conducted using the May 21st and June 8th SAR observations as they provided the highest quality observations of all provided images. To quantitatively explore the results using the model-observation hybrid frequencies, we can review the calculated RMSE and bias across the three transects used for analysis in chapter 3, results are shown in Table 3. Values that are an improvement over the prior bathymetry are highlighted in red. RMSE was improved across all transects except for transect B-B for the June 8th observations. The RMSE across transect A-A was reduced from 7.66 m in the prior bathymetry to 3.7 m in the posterior bathymetry for the June 8th image. When comparing the results using the hybrid data against the results of the model-derived observations, we can see that the model-derived observations performed better except for a minor improvement in transect C-C for June 8th.

Table 3: Root-mean-square-error and bias for MCR transects A-A, B-B, C-C after assimilation SAR wavenumber observations and model-observation hybrid frequencies

RMSE for Inversion Using Hybrid Data													
Assimilation	**Domain RMSE [m]**	**Transect RMSE [m]**			**Transect Bias [m]**			**Mean Transect Depth [m]**			**Mean Percent Error**		
		A-A	**B-B**	**C-C**	**A-A**	**B-B**	**C-C**	**A-A**	**B-B**	**C-C**	**A-A**	**B-B**	**C-C**
Prior	1.96	7.66	3.12	4.25	-3.89	0.52	1.80	22.56	16.89	10.41	33.94	18.49	40.83
21 MAY 13 13:47:33 UTC	**1.78**	**4.97**	**1.83**	**3.60**	-4.11	-0.45	-2.89				**22.01**	**10.84**	**34.60**
08 JUNE 13 02:14:14 UTC	**1.83**	**3.66**	3.36	**2.14**	0.48	1.95	-0.95				**16.22**	19.89	**20.55**

The resulting posterior bathymetry showed many strong similarities to the true bathymetry including; the navigational channel, Clatsop Spit, and Peacock Spit. Transect A-A shown in Figure 25d & 27d shows that the method is attempting to create the navigational channel; however it is underestimating the depth of the deeper sections of the channel. The cross channel transect C-C shown in Figures 25f & 27f show that the location and depth of the navigational channel is accurately predicted. Clatsop Spit is accurately represented in the posterior bathymetry in extent and location quite well; however the method has again underestimated the depth. Outside of the jetties, in the offshore direction, many of the shoals were underestimated, which is a reoccurring trend when the calculated true frequency is used for the inversion of other observation dates.

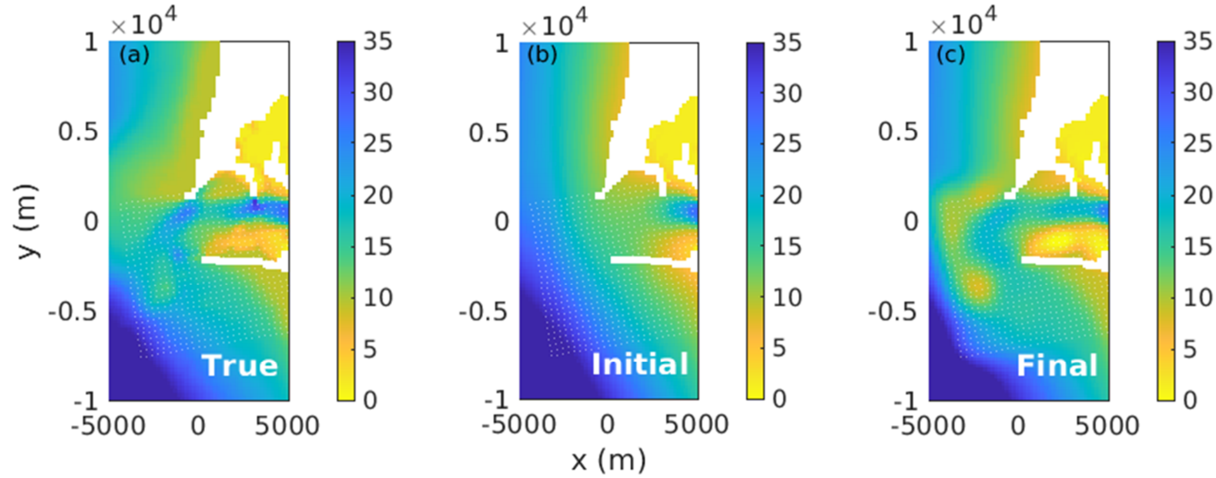

Figure 26: Results for assimilation using SAR observations and hybrid frequency for 21 May 2013 13:47:33 UTC (a) true bathymetry (b) Prior "smoothed" bathymetry and (c) posterior bathymetry

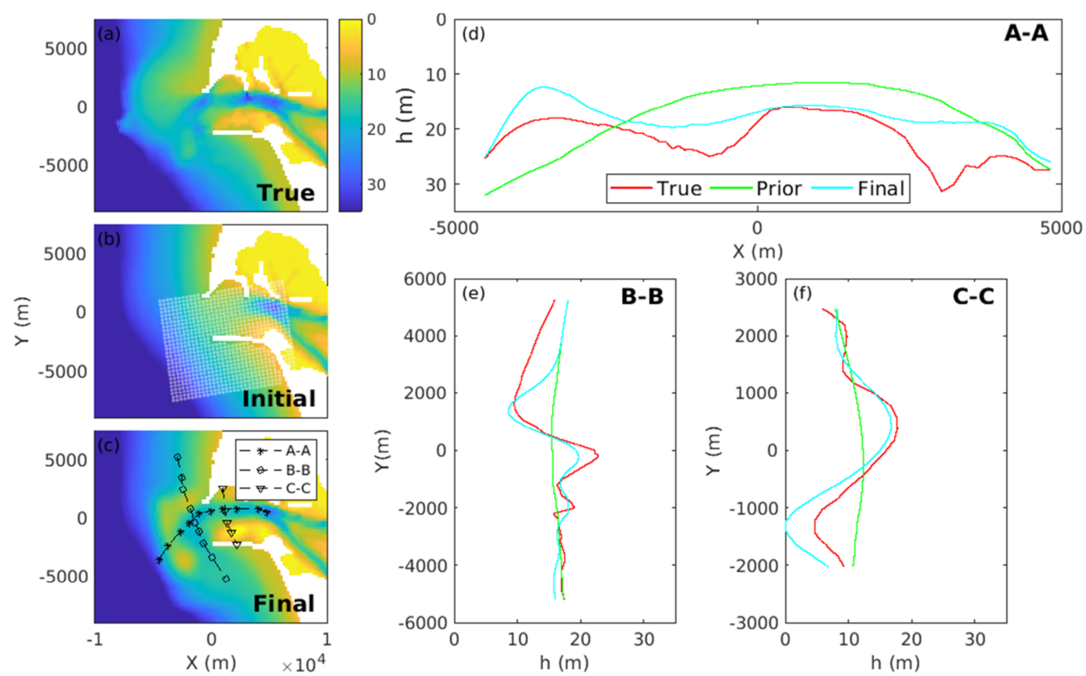

Figure 27: Results for assimilation using SAR observations and hybrid frequency for 21 May 2013 13:47:33 UTC (a) true bathymetry (b) Prior "smoothed" bathymetry and location of observations (c) posterior bathymetry and transects used for analysis (d) transect A-A (e) transect B-B (f) transect C-C

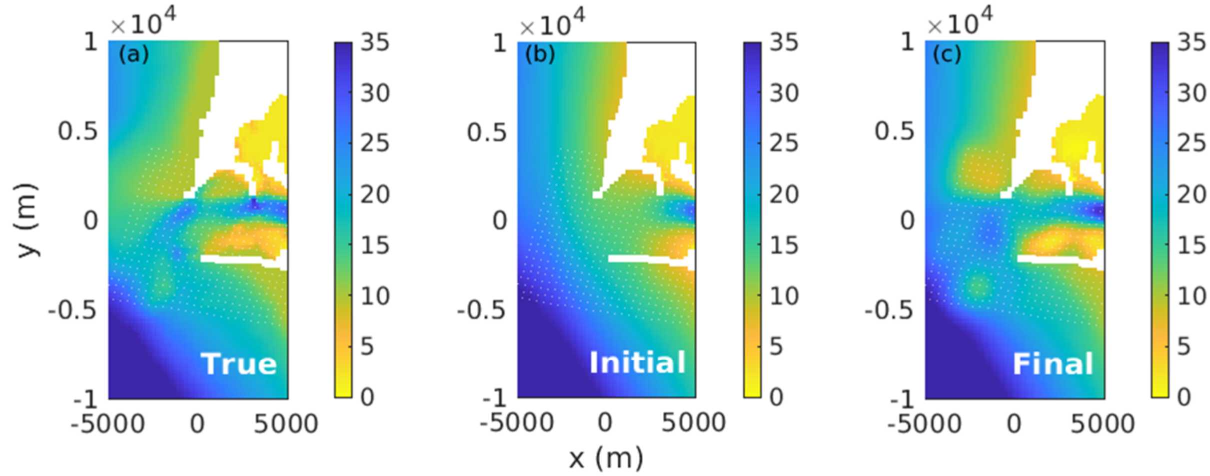

Figure 28: Results for assimilation using SAR observation and hybrid frequency for 08 JUNE 2013 02:14:14 UTC (a) true bathymetry (b) Prior "smoothed" bathymetry and (c) posterior bathymetry

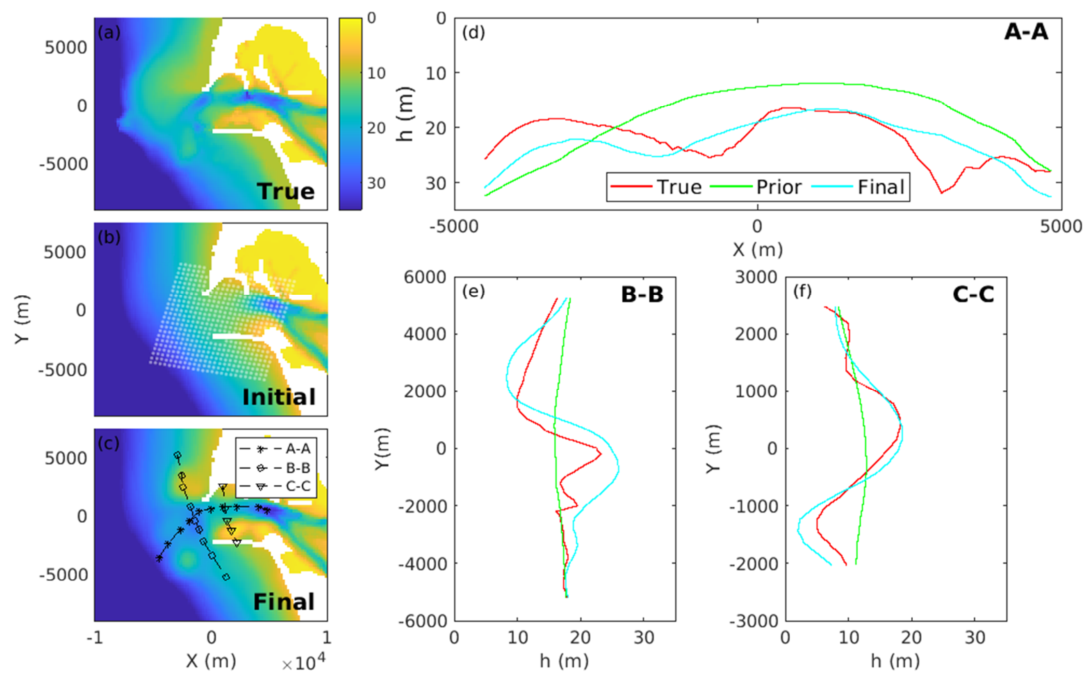

Figure 29: Results for assimilation using SAR observations and hybrid frequency for 08 JUNE 2013 02:14:14 UTC (a) true bathymetry (b) Prior "smoothed" bathymetry and location of observations (c) posterior bathymetry and transects used for analysis (d) transect A-A (e) transect B-B (f) transect C-C

4.2. Sensitivity to Assigned Frequency within Wave Direction Filter

Exploring the sensitivity of the assigned frequency to the assimilated wavenumber after it has been filtered by wave direction provided verification of the frequencies assimilated with the observations shown in Chapter 3. The May 21st and June 8th images were used for this analysis as they each contained the most observations in each wave direction filtering region. Only the results from the May 21st SAR image are shown in Figure 30, however similar results were seen for the June 8th observations. Each individual component (i.e. NW or SW region) associated with a frequency was used as the only observations assimilated in the inversion method while the frequency was varied across a range (0.0525 – 0.0775 Hz for the SW region and 0.0875-0.11 Hz for the NW region); the RMSE was then calculated for the estimated bathymetry across the three analyses transects. The RMSE analysis showed that for both May 21st and June 8th, the frequency determined by the NOAA buoy spectra (or a frequency very close to it) produced the best inversion results in a majority of the transects. Figure 30a & 30b shows the transect RMSE for the NW and SW regions for the May 21st image and illustrates that in transects A-A and B-B the RMSE is close to the minimum for the NOAA buoy observed frequency. Transect C-C shows an optimal frequency that is closer to 0.0925 Hz for the NW region. Figure 30c and 30d shows that the depth along transect A-A was underestimated with the NW and SW region observations. A possible explanation for this in regards to the SW region would be that majority of the SW region points are located outside of the jetty and to the south of the south jetty.

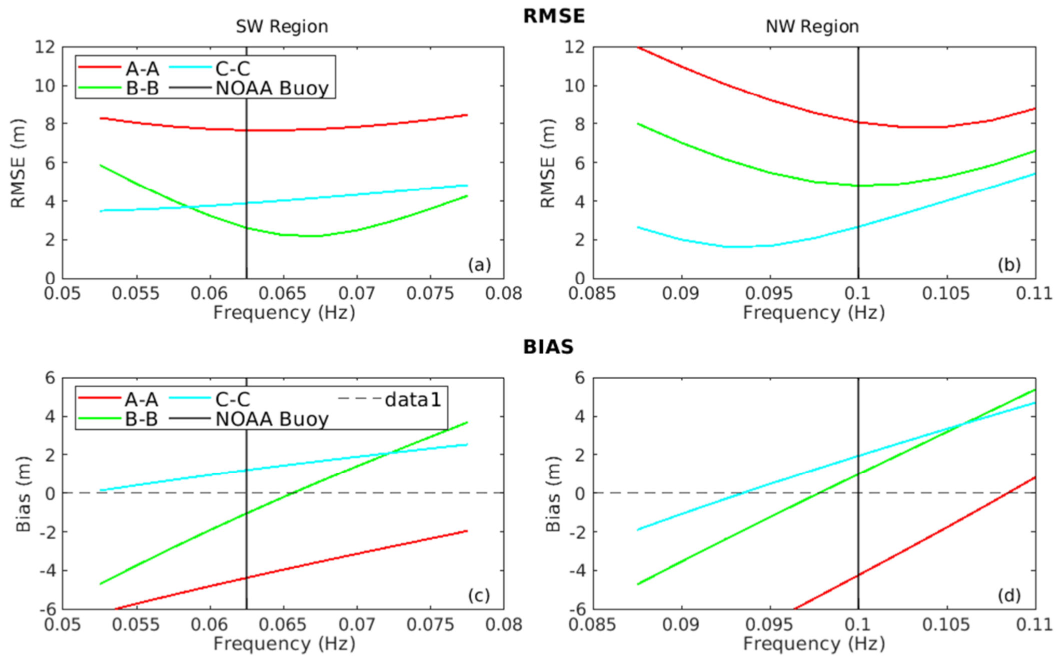

Figure 30: RMSE and bias for sensitivity analysis of frequency within wave direction filtering regions for May 21, 2013 13:47:33 UTC observations (a) RMSE for observation in the SW region of the wave direction filter (b) RMSE of observations in the NW Regions (c) bias for observation in the SW region of the wave direction filter (d) bias of observations in the NW Regions

4.3. Evaluation of Additional SAR Observations and Future Work

With a total of 36 SAR images available for the MCR, there is an opportunity to analyze additional images other than the four discussed within this thesis. We briefly evaluated the 32 other SAR images for assimilation, and determine that the May 21st and June 8th provides some of the highest quality observations of all the images. However, an in-depth analysis was not conducted for the additional images, and as such, there is an opportunity for future analysis of the SAR observation data set.

4.3.1 Additional Observation filtering

In addition to the wave direction filter method, a few other methods were applied to try and identify the highest quality observations. These filters were often situational and could not be applied across all the observations. For example, the SNR threshold was increased to 50 for all the images and this slightly reduced the RMSE for the

May 21st and June 8th images compared to the SNR threshold of 10 specified in Chapter 3. However, using a SNR threshold of 50 severely limited the number of observations available for assimilation along the navigational channel for May 29th & 30th. Results generated when a higher SNR threshold was used for the May 21st assimilation can be seen in Figures 31 & 32. In this assimilation, the SNR threshold was 50 and the wave direction filter regions were reduced in size. These changes in the quality filter reduced the RMSE in Transect A-A from 7.8 m to 4.2 m, while the RMSE in transect B-B and C-C remained the same. It is our belief that a filter with a higher quality threshold could be used to improve the posterior bathymetry and that this could be an opportunity for future exploration and analysis.

The posterior bathymetry often lacked a smooth transition between the numerous estimated holes and shoals; further analysis was conducted to understand the cause of these features. It was determined that often the hole or shoal was associated with a cluster of a few points that were associated with a wavenumber that was not consistent with what the model was estimating, thereby creating a deeper or shallower area about these few points. A technique to filter out these inconsistent points was not determined by this study but would be an opportunity for future work that could significantly reduce the RMSE of the posterior bathymetries estimated by the method.

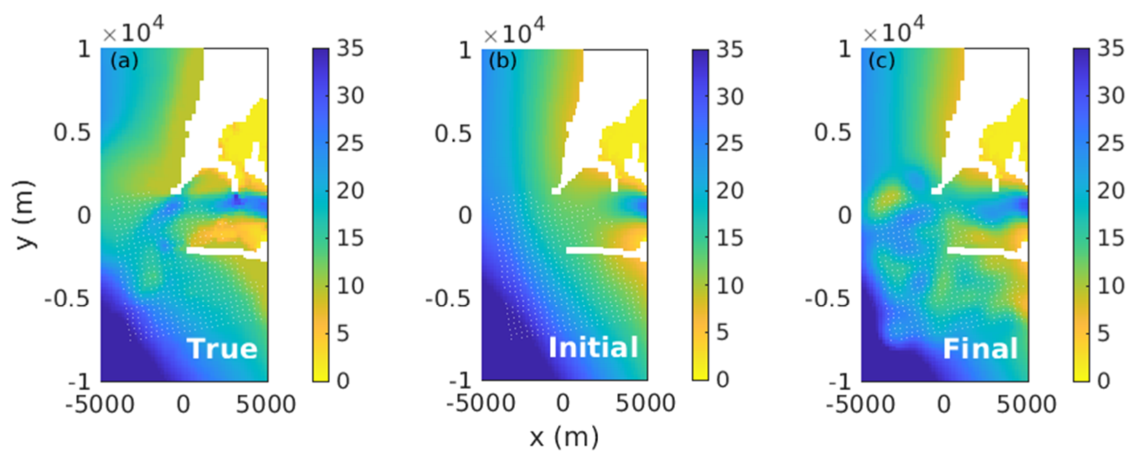

Figure 31: Results for assimilation using a higher SNR threshold and a more precise wave direction filter region for 21 May 2013 13:47:33 UTC (a) true bathymetry (b) Prior "smoothed" bathymetry and (c) posterior bathymetry

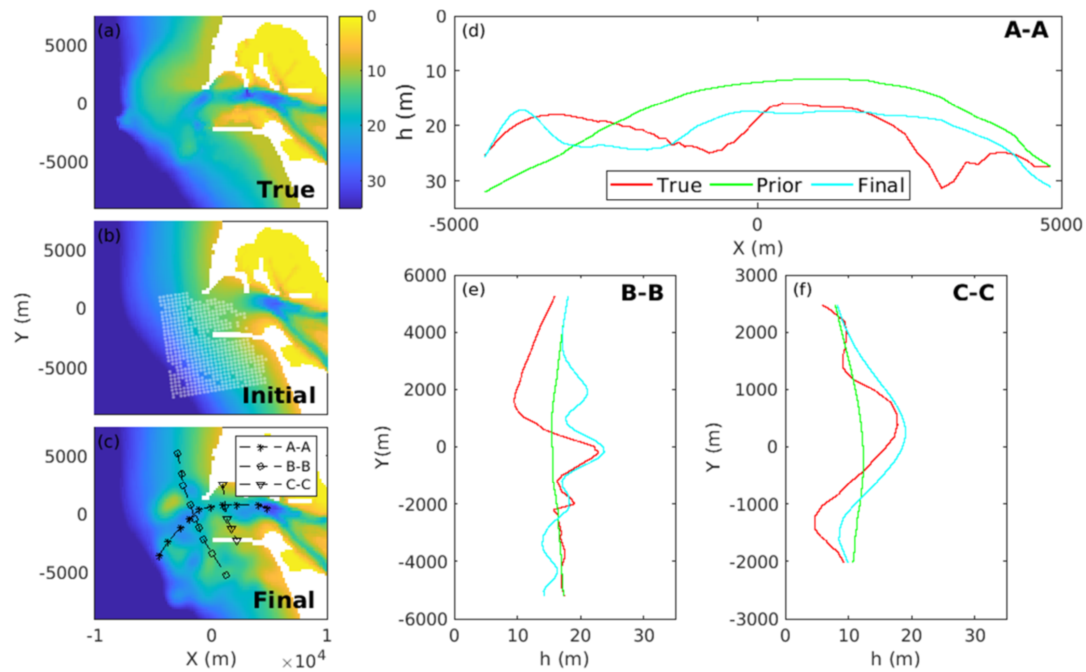

Figure 32: Results for assimilation using a higher SNR threshold and a more precise wave direction filter region for 21 May 2013 13:47:33 UTC (a) true bathymetry (b) Prior "smoothed" bathymetry and location of observations (c) posterior bathymetry and transects used for analysis (d) transect A-A

4.4. Limitations

The assimilation method described here and the associated results it generated are dependent on the quantity and quality of the observations being assimilated, therefore we have determined several limitations of the SAR observations when being used for bathymetry inversion at a tidal inlet. Firstly, spatial resolutions of the SAR observations can limit the ability of the inversion method; the overall spatial resolution of the SAR observations can have a window size as small as 64 x 64 pixels; however, this window size might not be small enough to provide the resolution of observations to estimate smaller spatial features in the bathymetry. Additionally, applying a quality filter to the data, such as SNR can remove a majority of the points in key areas of interest such as the navigational channel between the jetties or ODMDS A.

The presence of breaking waves in the SAR images led to a reduction of high quality observation points. This was especially noticeable in the May 29th image where a majority of the observation points in the area between the north and south jetty had a low SNR; these points were therefore not reliable for assimilation. The breaking waves are noticeable in the SAR image as the brighter portions of the image between the jetties. Additional discussion with Dr. Chris Wackerman confirmed that the presence of breaking waves produces lower quality observations because the SAR images the breaking waves to appear stationary.

In the event of future SAR observations for bathymetry inversion, this study provides the following recommendations based on the discussed results. The optimal conditions for observations would include a time period when there is limited wave breaking, multiple wave components are present with differing wave directions, and the arriving wave components contain waves with relatively longer wavelengths. In the case of the MCR and other inlets, observations collected during slack tide may reduce the impact of currents on wavelength and wave breaking.

Chapter 5: Conclusion

In this research we created and tested a methodology that assimilated wave characteristics collected via synthetic-aperture radar and model-generated surface currents to produce bathymetry estimates at the Mouth of the Columbia River. The important outcomes of this thesis are as follows:

1. Implemented an assimilation method that allowed for covariance matrices to be computed in the observational domain, thereby reducing the computational storage and efficiency and no longer required the covariance matrices to be calculated in the model domain.
2. Verified that assimilating model-derived SAR wavenumber observations and a single absolute angular frequency can produce an estimate bathymetry with a reduced RMSE when compared to a prior “best-guess” bathymetry.
3. Generated wavenumber-frequency pairs that reproduced many of the large scale features present in the true bathymetry by filtering wavenumber observations using wave direction and the frequency as measured by the NOAA buoy.
4. Produced posterior bathymetries that when observation conditions were favorable, provided a sense of the MCR navigational Channel, Peacock Spit, Clatsop Spit, and ODMDS A. RMSE was reduced across some of the analysis transect that were located along the key bathymetry features.
5. Explored the uncertainty related to assigning an absolute angular frequency to a wavenumber observation and how this uncertainty manifests itself as RMSE in the estimated posterior bathymetry. It was then confirmed that the angular frequency recorded by the NOAA buoy was very similar to the optimal frequency to associate with the SAR wavenumber observations for assimilation.
6. Recognized the limitations of this method involving SAR observations for data assimilation including the influence of wave breaking, spatial resolution

of observations, and the challenge of associating the correct frequency with the wavenumber observations.

Bibliography

Akan, Ç., McWilliams, J. C., Moghimi, S., & Özkan-Haller, H. T. (2018). Frontal dynamics at the edge of the Columbia River plume. *Ocean Modelling (Oxford)*, *122*, 1–12.

Akan, Ç., Moghimi, S., Özkan-Haller, H. T., Osborne, J., & Kurapov, A. (2017). On the dynamics of the Mouth of the Columbia River: Results from a three-dimensional fully coupled wave-current interaction model. *Journal of Geophysical Research: Oceans*, *122*(7), 5218–5236. https://doi.org/10.1002/2016JC012307

Barnard, P. L., Erikson, L., Rubin, D. M., Dartnell, P., & Kvitek, R. G. (2012). Analyzing Bedforms Mapped Using Multibeam Sonar to Determine Regional Bedload Sediment Transport Patterns in the San Francisco Bay Coastal System. *Sediments, Morphology and Sedimentary Processes on Continental Shelves*, *2012*, 273–294. https://doi.org/10.1002/9781118311172.ch13

Booij, N., Ris, R. C., & Holthuijsen, L. H. (1999). A third-generation wave model for coastal regions: 1. Model description and validation. *Journal of Geophysical Research: Oceans*, *104*(C4), 7649–7666.

Elias, E. P. L., Gelfenbaum, G., & Van Der Westhuysen, A. J. (2012). Validation of a coupled wave-flow model in a high-energy setting: The mouth of the Columbia River. *Journal of Geophysical Research: Oceans*, *117*(9), 1–21. https://doi.org/10.1029/2012JC008105

Ellenson, A., & Özkan-Haller, H. T. (2018). Predicting Large Ocean Wave Events Characterized by Bimodal Energy Spectra in the Presence of a Low-Level Southerly Wind Feature. *Weather and Forecasting*, *33*(2), 479–499.

Evensen, G. (2007). *Data assimilation : the ensemble Kalman filter*. Springer.

Gailani, J., Brutsché, K. E., Godsey, E., Wang, P., & Hartman, M. A. (2019). *Dredged Material Coastal and Hydraulics Laboratory*.

Gailani, J. Z., Smith, J. W., Kraus, N. C., Mcgee, D. D., Hands, E. B., Mayers, C. J., Moritz, H. R., Moritz, H. P., Siipola, M. D., Daryl, B., Byrnes, M. R., Li, F., Dibble, T. L., Hollings, W. H., Lund, C. R., Sollitt, C. K., & Standley, D. R. (2003). *Monitoring Dredged Material Disposal at Mouth of Columbia River, Washington/Oregon, USA* (Issue July).

Gelfenbaum, G., MacMahan, J., & Reniers, A. (2013). *Field and Numerical Study of the Columbia River Mouth*.

Gonzalez, F. I., Cokelet, E. D., Gower, J. F. R., & Mulhern, M. R. (1985). SLAR and In-Situ Observations of Wave-Current Interaction on the Columbia River Bar. In Y. Toba & H. Mitsuyasu (Eds.), *The Ocean Surface: Wave Breaking, Turbulent Mixing and Radio Probing* (pp. 303–310). Springer Netherlands. https://doi.org/10.1007/978-94-015-7717-5_41

Holman, R., Plant, N., & Holland, T. (2013). CBathy: A robust algorithm for estimating nearshore bathymetry. *Journal of Geophysical Research: Oceans*, *118*(5), 2595–2609. https://doi.org/10.1002/jgrc.20199

Honegger, D. A., Haller, M. C., & Holman, R. A. (2019). High-resolution bathymetry estimates via X-band marine radar: 1. beaches. *Coastal Engineering*, *149*(March), 39–48. https://doi.org/10.1016/j.coastaleng.2019.03.003

Honegger, D. A., Haller, M. C., & Holman, R. A. (2020). High-resolution bathymetry estimates via X-band marine radar: 2. Effects of currents at tidal inlets. *Coastal Engineering*, *156*(December 2019), 103626. https://doi.org/10.1016/j.coastaleng.2019.103626

Kaminsky, G. M., Ruggiero, P., Buijsman, M. C., McCandless, D., & Gelfenbaum, G. (2010). Historical evolution of the Columbia River littoral cell. *Marine Geology*, *273*(1–4), 96–126. https://doi.org/10.1016/j.margeo.2010.02.006

Landon, K. C., Wilson, G. W., Özkan-Haller, H. T., & MacMahan, J. H. (2014). Bathymetry estimation using drifter-based velocity measurements on the Kootenai River, Idaho. *Journal of Atmospheric and Oceanic Technology*, *31*(2), 503–514. https://doi.org/10.1175/JTECH-D-13-00123.1

Lyzenga, D. R. (1988). An analytic representation of the synthetic aperture radar image spectrum for ocean waves. *Journal of Geophysical Research: Oceans*, *93*(C11), 13859–13865. https://doi.org/10.1029/JC093iC11p13859

Moghimi, S., Özkan-Haller, H. T., Wilson, G. W., & Kurapov, A. (2016). Data assimilation for bathymetry estimation at a tidal inlet. *Journal of Atmospheric and Oceanic Technology*, *33*(10), 2145–2163. https://doi.org/10.1175/JTECH-D-14-00188.1

Moritz, H. R., Byrnes, M. R., & Griffee, S. F. (2007). Engineering activities influencing historical sediment transport pathways at the Columbia River Mouth, WA/OR. *Coastal Sediments '07 - Proceedings of 6th International Symposium on Coastal Engineering and Science of Coastal Sediment Processes*, 1–14. https://doi.org/10.1061/40926(239)138

Plant, N. G., Holland, K. T., & Haller, M. C. (2008). Ocean wavenumber estimation from wave-resolving time series imagery. *IEEE Transactions on Geoscience and Remote Sensing*, *46*(9), 2644–2658. https://doi.org/10.1109/TGRS.2008.919821

Ruggiero, P., Kaminsky, G. M., Gelfenbaum, G., & Voigt, B. (2005). Seasonal to interannual morphodynamics along a high-energy dissipative littoral cell. *Journal of Coastal Research*, *21*(3), 553–578. https://doi.org/10.2112/03-0029.1

Shchepetkin, A. F., & McWilliams, J. C. (2003). A method for computing horizontal pressure-gradient force in an oceanic model with a nonaligned vertical coordinate. *Journal of Geophysical Research - Oceans*, *108*(C3), 3090--n/a.

Shchepetkin, A. F., & McWilliams, J. C. (2005). The regional oceanic modeling system (ROMS): a split-explicit, free-surface, topography-following-coordinate oceanic model. *Ocean Modelling (Oxford)*, *9*(4), 347–404.

Tillotson, K., & Komar, P. D. (1997). The wave climate of the Pacific Northwest (Oregon and Washington): A comparison of data sources. *Journal of Coastal Research*, *13*(2), 440–452.

USACE. (2012). *Major Rehabilitation Evaluation Report: Columbia River at the Mouth , Oregon and Washington: Major Rehabilitation of the Jetty System at the Mouth of the Columbia River* (Issue June).

Warner, J. C., Armstrong, B., He, R., & Zambon, J. B. (2010). Development of a Coupled Ocean–Atmosphere–Wave–Sediment Transport (COAWST) Modeling System. *Ocean Modelling (Oxford)*, *35*(3), 230–244.

Wilson, G., & Özkan-haller, H. T. (2012). Ensemble-based data assimilation for estimation of river depths. *Journal of Atmospheric and Oceanic Technology*, *29*(10), 1558–1568. https://doi.org/10.1175/JTECH-D-12-00014.1

Wilson, G. W., Özkan-Haller, H. T., Holman, R. A., Haller, M. C., Honegger, D. A., & Chickadel, C. C. (2014). Surf zone bathymetry and circulation predictions via data assimilation of remote sensing observations. *Journal of Geophysical Research: Oceans*, *119*(3), 1993–2016. https://doi.org/10.1002/2013JC009213

Wilson, Greg W., Özkan-Haller, H. T., & Holman, R. A. (2010). Data assimilation and bathymetric inversion in a two-dimensional horizontal surf zone model. *Journal of Geophysical Research: Oceans*, *115*(12), 1–17. https://doi.org/10.1029/2010JC006286

Yu, P., Johannessen, J. A., Kudryavtsev, V., Zhong, X., & Zhou, Y. (2016). Journal of Geophysical Research: Oceans. *Journal of Geophysical Research: Oceans*, *121*(5), 3010–3028. https://doi.org/10.1002/2015JC011516

Zuckerman, S., & Anderson, S. (2018). Bathymetry and water-level estimation using x-band radar at a tidal inlet. *Journal of Coastal Research*, *34*(5), 1227–1235. https://doi.org/10.2112/JCOASTRES-D-17-00182.1

Appendix

Appendix A. Bathymetric Inversion Code

```
% Assimilate SAR oobservation data Provided by Chris Wackerman at NRL
% Code was updated 3/30/17 to impliment unique frequency values at
 each
% oberservation point

tic
clear
addpath(...
    ['/home/server/pi/homes/sharper/Documents/MCR Matlab/Matlab/'...
    'SHH_matlab_functions']);


%-------------------------------------------------------------------------
% INPUT

% Parameters for model area of influence
S = 10;
lx = 800;
ly = lx;
% Observation parameters for area of influence
So = 0.007;
Lxo = 200;
Lyo = Lxo;

% Indices that controls space and time domain
l1yind = 137;
l2yind = 125;
l3xind = 58;
l4xind = 30;

ind_t = 989;            % NEEDS TO BE UPDATED FOR NEW MODEL RUN Index
                        % for time for true bathy
ind_x = [100 180];      % Index offsets [from_begin from end]
ind_y = [25 25];        % for example [10 10] means we start at index
 11 and
ind_xo = [0 0];         % end at index end-10. ind_x and ind_y are for
 true
ind_yo = [0 0];         % bathy while ind_xo and ind_yo are for
 observations
cs = flipud(parula);    % setting plotting colormap


% File paths for true and prior model runs
mainpathtrue = '/home/server/pi/homes/sharper/Documents/MCR
 Matlab/'...
    'Matlab/Inversion/21MAY13_134733/21MAY13_Truth';
mainpathprior = '/home/server/pi/homes/sharper/Documents/MCR
 Matlab/'...
    'Matlab/Inversion/21MAY13_134733/21MAY13_Prior';

tr_grd = [mainpathtrue,'/mcr_200m_2013_grd_v1.nc']; %Grid from true
 bathy
```

```
tr_depth = [mainpathtrue,'/depth.nc']; % depth from true bathy (SWAN)
tr_vel = [mainpathtrue,'/vel.nc']; %velocity from true bathy (SWAN)
tr_wdir = [mainpathtrue,'/wdir.nc']; % wave direction from true
 bathy(SWAN)
pr_depth = [mainpathprior,'/depth.nc']; % depth from prior bathy
 (SWAN)
pr_vel = [mainpathprior,'/vel.nc']; %velocity from prior bathy (SWAN)
pr_wdir = [mainpathprior,'/wdir.nc']; % wave direction from prior
 bathy(SWAN)

% Plotting controls
cl = [0 35]; % setting color bar axis limits

%------------------------------------------------------------------------
% MAIN CODE

% Load/read from files
load('SAR_SNF10_WDF_21MAY13_134733_500m_sc09_Thesis.mat');
filename1 = ('SAR_assim_21MAY13_134733_WDF_Thesis_f1.png');
filename2 = ('SAR_assim_21MAY13_134733_WDF_Thesis_f2.png');
filename3 = ('SAR_assim_21MAY13_134733_WDF_RMSE_thesis_data.mat');


hgrdt = ncread(tr_depth,'depth');
hgrdm = ncread(pr_depth,'depth');
lat = ncread(tr_grd,'lat_rho');
lon = ncread(tr_grd,'lon_rho');
ut = ncread(tr_vel,'xcur');
vt = ncread(tr_vel,'ycur');
u = ncread(pr_vel,'xcur');
v = ncread(pr_vel,'ycur');
thetat = ncread(tr_wdir,'theta0');
theta = ncread(pr_wdir,'theta0');



% True bathy
time = ncread(tr_vel,'time');
time_datetime = datetime(time,'ConvertFrom','posixtime');
disp('Using true bathy at time')
disp(time_datetime(ind_t))
[xgrdt,ygrdt] = lltoxy_MCR(lat,lon);
xgrdt = xgrdt(1+ind_x(1):end-ind_x(2),1+ind_y(1):end-ind_y(2));
ygrdt = ygrdt(1+ind_x(1):end-ind_x(2),1+ind_y(1):end-ind_y(2));
hgrdt = hgrdt(1+ind_x(1):end-ind_x(2),1+ind_y(1):end-ind_y(2),ind_t);
ut = ut(1+ind_x(1):end-ind_x(2),1+ind_y(1):end-ind_y(2),ind_t);
vt = vt(1+ind_x(1):end-ind_x(2),1+ind_y(1):end-ind_y(2),ind_t);
thetat = thetat(1+ind_x(1):end-ind_x(2),1+ind_y(1):end-
ind_y(2),ind_t);

% SAR Observation Data import
% SAR data was pre processed in a Data Import script
xgrdo = SARdata_21MAY13.x_MCR; % X-location
ygrdo = SARdata_21MAY13.y_MCR; % y-location
```

```
xgrdo = double(xgrdo);
ygrdo = double(ygrdo);
ko = SARdata_21MAY13.kmag; %Wavenumber from SAR Observations

% Interpolating the true depth grid at the observation points
F = scatteredInterpolant(xgrdt(:),ygrdt(:),hgrdt(:));
F.ExtrapolationMethod = 'none';
hgrdo = F(xgrdo,ygrdo);
ind_grdo = ~isnan(hgrdo);
xo = xgrdo(ind_grdo);
yo = ygrdo(ind_grdo);
ko = ko(ind_grdo);


%Frequency input
f = SARdata_21MAY13.NOAA_Freq(ind_grdo); % Frequency



% Model (from smoothed "prior" bathy)
time = ncread(pr_depth,'time');
time_datetime = datetime(time,'ConvertFrom','posixtime');
disp('Using prior bathy at time')
disp(time_datetime(ind_t))
hgrdm = hgrdm(1+ind_x(1):end-ind_x(2),1+ind_y(1):end-ind_y(2),ind_t);
up = u(1+ind_x(1):end-ind_x(2),1+ind_y(1):end-ind_y(2),ind_t);
vp = v(1+ind_x(1):end-ind_x(2),1+ind_y(1):end-ind_y(2),ind_t);
thetap = theta(1+ind_x(1):end-ind_x(2),1+ind_y(1):end-ind_y(2),ind_t);

% Interpolate prior bathy data at observation points
F = scatteredInterpolant(xgrdt(:),ygrdt(:),hgrdm(:));
F.ExtrapolationMethod = 'none';
hgrdop = F(xo,yo);
F = scatteredInterpolant(xgrdt(:),ygrdt(:),up(:));
uop = F(xo,yo);
F = scatteredInterpolant(xgrdt(:),ygrdt(:),vp(:));
vop = F(xo,yo);
F = scatteredInterpolant(xgrdt(:),ygrdt(:),thetap(:));
thetaop = 270 - F(xo,yo);
kbarxp = cosd(thetaop);
kbaryp = sind(thetaop);
sigma = 2*pi*f;


ind_grdm = ~isnan(thetap);
hp = hgrdm(ind_grdm);

x = xgrdt(ind_grdm);
y = ygrdt(ind_grdm);


% Get updated bathy
% M = Number of observation points
% N = Number of model points
```

```
k = disper(sigma,hgrdop,uop,vop,kbarxp,kbaryp);
% [M x 1] solve the dispersion relationship for the
%prior bathymetry using the model outputs
dkdh = get_dkdh(sigma,k,hgrdop,uop,vop,kbarxp,kbaryp);
% [M x N] sensitivuty of k to h-pertibations about prior depth
Coo = get_Co(xo,yo,S,lx,ly);
% [M x M] covariance matrix between bathymetry at observation points
Coh = get_Coh(xo,yo,x,y,S,lx,ly);
%[M x N] prior bathymetry error covariance - covariance between depth
 at
% observation points vs depth at model grid points
Co = get_Co(xo,yo,So,Lxo,Lyo);
% [M x M] observation error covariance matric

A = Coh'*diag(dkdh); % [N x M]
B = diag(dkdh)*Coo*diag(dkdh); % [M x M]
D = ko-k; % [M x 1]

del_h = A*((B +Co)^-1)* D;
h = hp + del_h;

toc


%------------------------------------------------------------------------
```

PLOTTING

```
close all
f = figure;
set(f,'Position', get(0, 'Screensize'));
set(f,'WindowState','maximized')
set(f,'Renderer', 'opengl')
ax = subplot(1,3,1);
hold on
pcolor(xgrdt,ygrdt,hgrdt)
shading flat
colormap(cs)
colorbar
caxis(cl)
% xlabel('x (m)')
ylabel('y (m)')
% scatter(xt,yt,1,'.')
scatter(xo,yo,5,'w','.','MarkerEdgeAlpha',0.5)
text(0.95,0.1,'True','Units','normalized','FontSize',16,...
    'HorizontalAlignment','Right','Color','w','FontWeight','bold')
axis equal tight
ax.FontSize = 14;
xlim([-5000 5000])
ylim([-10000 10000])
box on
dim = [.13 .43 .5 .3];
str = '(a)';
```

```
annotation('textbox',dim,'String',str,'FitBoxToText','on','FontSize',
 12, ...
    'LineStyle','none');


ax = subplot(1,3,2);
hold on
pcolor(xgrdt,ygrdt,hgrdm)
caxis(cl)
xlabel('x (m)')
% ylabel('y (m)')
colorbar
shading flat
scatter(xo,yo,5,'w','.','MarkerEdgeAlpha',0.5)
text(0.95,0.1,'Initial','Units','normalized','FontSize',16,...
    'HorizontalAlignment','Right','Color','w','FontWeight','bold')
axis equal tight
ax.FontSize = 14;
xlim([-5000 5000])
ylim([-10000 10000])
box on
dim = [.41 .43 .5 .3];
str = '(b)';
annotation('textbox',dim,'String',str,'FitBoxToText','on','FontSize',
 12, ...
    'LineStyle','none');


hgrdu = hgrdm;
hgrdu(ind_grdm) = h;
ax = subplot(1,3,3);
hold on
pcolor(xgrdt,ygrdt,hgrdu)
caxis(cl)
colorbar
shading flat
% xlabel('x (m)')
% ylabel('y (m)')
scatter(xo,yo,5,'w','.','MarkerEdgeAlpha',0.5)
text(0.95,0.1,'Final','Units','normalized','FontSize',16,...
    'HorizontalAlignment','Right','Color','w','FontWeight','bold')
axis equal tight
ax.FontSize = 14;
xlim([-5000 5000])
ylim([-10000 10000])
box on
dim = [.69 .43 .5 .3];
str = '(c)';
annotation('textbox',dim,'String',str,'FitBoxToText','on','FontSize',
 12,...
    'LineStyle','none');
f.InvertHardcopy = 'off';
f.Color = 'white';
F = getframe(f);
```

```
% pause(5);
imwrite(F.cdata, filename1,'png')


% RMSE Transects
T1x = [-4490 -3664 -2636 -1817 -998.5 10.01 1019 2224 4033 4833];
T1y = [-3551 -2361 -1173 -383.3 406.7 593.3 780 763.9 740.3 529.6];

T2x = [-2917 -2549 -2367 -1795 -1416 -1029 -645.9 135.1 1307];
T2y = [5242 3433 2429 818.4 -388.9 -1196 -2202 -3415 -5234];

T3x = [1043 1225 1407 1794 2200];
T3y = [2554 550.4 -453.6 -1260 -2272];

T1x_interp = linspace(min(T1x),max(T1x),10000);
T1y_interp = interp1(T1x,T1y,T1x_interp);

T2x_interp = linspace(min(T2x),max(T2x),10000);
T2y_interp = interp1(T2x,T2y,T2x_interp);

T3x_interp = linspace(min(T3x),max(T3x),10000);
T3y_interp = interp1(T3x,T3y,T3x_interp);

F_true = scatteredInterpolant(xgrdt(:),ygrdt(:),hgrdt(:));
F_prior = scatteredInterpolant(xgrdt(:),ygrdt(:),hgrdm(:));
F_final = scatteredInterpolant(xgrdt(:),ygrdt(:),hgrdu(:));
T1z_true = F_true(T1x_interp,T1y_interp);
T1z_prior = F_prior(T1x_interp,T1y_interp);
T1z_final = F_final(T1x_interp,T1y_interp);


T2z_true = F_true(T2x_interp,T2y_interp);
T2z_prior = F_prior(T2x_interp,T2y_interp);
T2z_final = F_final(T2x_interp,T2y_interp);


T3z_true = F_true(T3x_interp,T3y_interp);
T3z_prior = F_prior(T3x_interp,T3y_interp);
T3z_final = F_final(T3x_interp,T3y_interp);



f1 = figure;
set(f1,'Position', get(0, 'Screensize'));
set(f1,'WindowState','maximized')
set(f1,'Renderer', 'opengl')
ax = axes;
hold on
pcolor(xgrdt,ygrdt,hgrdt);
c = colorbar;
caxis(cl);
% xlabel('x (m)')
% ylabel('y (m)')
% xlim([-5000 5000])
```

```
% ylim([-10000 10000])
text(0.95,0.1,'True','Units','normalized','FontSize',16,...
     'HorizontalAlignment','Right','Color','k','FontWeight','bold')
shading flat
colormap(cs);
box on
c.Label.String = 'h (m)';
c.Label.FontSize = 15;
c.Direction = 'reverse';
f1.Units = 'inches';
% f1.Position = [0,0,10,5.8];
ax.FontSize = 12;
ax.Position = [0.05 0.70 0.3 0.29];
set(gca,'XtickLabel',[]);
axis equal
xlim([-10000 10000])
ylim([-9000 7500])
dim = [.09 .69 .5 .3];
str = '(a)';
annotation('textbox',dim,'String',str,'FitBoxToText','on','FontSize',
 12,...
    'LineStyle','none');


ax = axes;
hold on
pcolor(xgrdt,ygrdt,hgrdm)
caxis(cl)
% xlabel('x (m)')
ylabel('Y (m)')
xlim([-5000 5000])
ylim([-10000 10000])
text(0.95,0.1,'Initial','Units','normalized','FontSize',16,...
    'HorizontalAlignment','Right','Color','k','FontWeight','bold')
shading flat
colormap(c);
box on
s =
 scatter(xo,yo,'w','.','MarkerEdgeAlpha',0.5,'DisplayName','Observations');
ax.FontSize = 12;
ax.Position = [0.05 0.39 0.3 0.29];
set(gca,'XtickLabel',[]);
axis equal
xlim([-10000 10000])
ylim([-9000 7500])
dim = [.09 .38 .5 .3];
str = '(b)';
annotation('textbox',dim,'String',str,'FitBoxToText','on','FontSize',
 12,...
    'LineStyle','none');



ax = axes;
```

```
hold on
caxis(cl)
xlabel('X (m)')
% ylabel('y (m)')
xlim([-5000 5000])
ylim([-10000 10000])
text(0.95,0.1,'Final','Units','normalized','FontSize',16,...
    'HorizontalAlignment','Right','Color','k','FontWeight','bold')
pl(1) = pcolor(xgrdt,ygrdt,hgrdu);
shading flat
pl(4) = plot(T1x,T1y,'--k*','DisplayName','A-A',...
    'LineWidth',0.1,'MarkerSize',5);
pl(5) = plot(T2x,T2y,'--ko','DisplayName','B-B',...
    'LineWidth',0.1,'MarkerSize',5);
pl(6) = plot(T3x,T3y,'--kv','DisplayName','C-C',...
    'LineWidth',0.1,'MarkerSize',5);
shading flat
colormap(c);
lg = legend(pl([4 5 6]));
lg.FontSize = 10;
lg.Location = 'northeast';
box on
ax.FontSize = 12;
ax.Position = [0.05 0.08 0.3 0.29];
axis equal
xlim([-10000 10000])
ylim([-9000 7500])
dim = [.09 .07 .5 .3];
str = '(c)';
annotation('textbox',dim,'String',str,'FitBoxToText','on','FontSize',
 12,...
    'LineStyle','none');


ax = axes;
lg = legend;
hold on
xlabel('X (m)')
plot(T1x_interp,T1z_true,'r','DisplayName','True','LineWidth',...
    1.5);
plot(T1x_interp,T1z_prior,'g','DisplayName','Prior','LineWidth',...
    1.5);
plot(T1x_interp,T1z_final,'c','DisplayName','Final','LineWidth',...
    1.5);
ylim(cl);
text(0.98,0.93,'A-A','Units','normalized',...
    'FontSize',16,'Color','k',...,
    'FontWeight','bold','HorizontalAlignment','right')
box on
ax.Position = [0.42 0.7 0.55 0.29];
ax.FontSize = 12;
% ax.XTickLabel = [];
ax.YDir = 'reverse';
lg.FontSize = 14;
```

```
lg.NumColumns = 3;
lg.Location = 'south';
dim = [.42 .69 .5 .3];
str = '(d)';
annotation('textbox',dim,'String',str,'FitBoxToText','on','FontSize',
 12,...
    'LineStyle','none');


ax = axes;
hold on
xlabel('x (m)')
ylabel('h (m)')
plot(T2z_true,T2y_interp,'r','DisplayName','True','LineWidth',...
    1.5);
plot(T2z_prior,T2y_interp,'g','DisplayName','Prior','LineWidth',...
    1.5);
plot(T2z_final,T2y_interp,'c','DisplayName','Final','LineWidth',...
    1.5);
xlim(cl);
text(0.95,0.95,'B-B','Units','normalized',...
    'FontSize',16,'Color','k',...,
    'FontWeight','bold','HorizontalAlignment','right')
box on
xlabel('h (m)');
ylabel('Y(m)');
ax.Position = [0.42 0.08 0.2 0.52];
ax.FontSize = 12;
% ax.YDir = 'reverse';
dim = [.42 .3 .5 .3];
str = '(e)';
annotation('textbox',dim,'String',str,'FitBoxToText','on','FontSize',
 12,...
    'LineStyle','none');



ax = axes;
hold on
box on
xlabel('h (m)')
ylabel('Y (m)')
plot(T3z_true,T3y_interp,'r','DisplayName','True','LineWidth',...
    1.5);
plot(T3z_prior,T3y_interp,'g','DisplayName','Prior','LineWidth',...
    1.5);
plot(T3z_final,T3y_interp,'c','DisplayName','Final','LineWidth',...
    1.5);
xlim(cl);
text(0.95,0.95,'C-C','Units','normalized',...
    'FontSize',16,'Color','k',...,
    'FontWeight','bold','HorizontalAlignment','right')

ax.Position = [0.72 0.08 0.2 0.52];
```

```
ax.FontSize = 14;
ax.XTick = [0,10,20,30];
ax.FontSize = 12;
dim = [.72 .3 .5 .3];
str = '(f)';
annotation('textbox',dim,'String',str,'FitBoxToText','on','FontSize',
 12,...
    'LineStyle','none');
f1.InvertHardcopy = 'off';
f1.Color = 'white';
F = getframe(f1);
% pause(10)
imwrite(F.cdata, filename2,'png')


close all

F = scatteredInterpolant(xgrdt(:),ygrdt(:),hgrdu(:));
F.ExtrapolationMethod = 'none';
hfinal = F(xo,yo);
RMSE = sqrt(mean(((hgrdt(:) - hgrdu(:)).^2),'omitnan'));


save(filename3,'RMSE','hgrdu','xgrdt','ygrdt','xo','yo','hfinal','hgrdop',...
    'hgrdm','hgrdt')
```

SUBROUTINES

```
function dkdh = get_dkdh(sigma,k,h,u,v,kbarx,kbary)

% sigma has size [1,N]
% h, u, v, kbarx, kbary has size [1,N]
% k has size [1,N]
% dkdh has size [N,N]

g = 9.81;

% compute dkdh
dkdh = -k.^2.*sech(k.*h).^2./(tanh(k.*h)+k.*h.*sech(k.*h).^2+2/
g.*(sigma- ...
    (u.*kbarx+v.*kbary).*k).*(u.*kbarx+v.*kbary));
% dkdh = diag(dkdh);

end

function k = disper(sigma,h,u,v,kbarx,kbary)

% sigma has size [1,N]
% h, u, v, kbarx, kbary has size [1,N]
% k has size [1,N]

g = 9.81;
```

```
% initial guess V&A 2013
kh_0 = sigma.^2.*h./g;
k = (kh_0+kh_0.^2.*exp(-(1.835+1.225.*kh_0.^1.35)))./
sqrt(tanh(kh_0))./h;

% iterate for better solution
for i = 1:5
    f = sigma.^2-2.*sigma.*(u.*kbarx+v.*kbary).*k+(u.*kbarx
+v.*kbary).^2 ...
        .*k.^2-g*k.*tanh(k.*h);
    fp = -2.*(sigma-(u.*kbarx+v.*kbary).*k).*(u.*kbarx+v.*kbary)- ...
        g*(tanh(k.*h)+k.*h.*sech(k.*h).^2);
    k = k-f./fp;
end

err = abs(f./fp);
disp(['Dispersion solver max error = ' num2str(max(err))])

end


function Co = get_Co(x,y,S,lx,ly)

Co = zeros(length(x));

for i = 1:length(x)
    for j = 1:length(x)
        Co(i,j) = S^2*exp(-(x(i)-x(j))^2/2/lx^2-(y(i)-y(j))^2/2/ly^2);
    end
end

end

function Coh = get_Coh(xo,yo,x,y,S,lx,ly)

Coh = zeros(length(xo),length(x));

for i = 1:length(xo)
    for j = 1:length(x)
        Coh(i,j) = S^2*exp(-(xo(i)-x(j))^2/2/lx^2-(yo(i)-y(j))^2/2/
ly^2);
    end
end

end

function Chh = get_Chh(x,y,S,lx,ly)

% x, y has size [1,N]
% S, lx, ly has size [1,1]
% Chh has size [N,N]

Chh = zeros(length(x));
```

```
for i = 1:length(x)
    for j = 1:length(x)
        Chh(i,j) = S^2*exp(-(x(i)-x(j))^2/2/lx^2-(y(i)-y(j))^2/2/
ly^2);
    end
end

end
```

Published with MATLAB® R2019b

.